Strong Gravitational Lensing and Multiwavelength Analysis of Groups of Galaxies: Characterising Intermediate Scale Dark Matter Structures

Auteur : Savonet, Robin
Promoteur(s) : Mahler, Guillaume; Sluse, Dominique
Faculté : Faculté des Sciences
Diplôme : Master en sciences spatiales, à finalité approfondie
Année académique : 2025-2026
URI/URL : http://hdl.handle.net/2268.2/25604

University of Liège
Faculty of Sciences
Department of astrophysics, geophysics and oceanography

Strong Gravitational Lensing and Multiwavelength Analysis of Groups of Galaxies: Characterising Intermediate-Scale Dark Matter Structures

---

SAVONET Robin

Master's thesis completed in order to obtain the degree of:
Master in Space Sciences, research focus (15 CTS)

Thesis supervisors:
MAHLER Guillaume
SLUSE Dominique

Reading committee:
GRODENT Denis
NADDAF MOGHADDAM Mohammad Hassan

Academic year 2025 - 2026

Abstract

Galaxy groups, with halo masses in the range 10^{13}-$10^{14}\,M_{\odot}$, occupy a critical intermediate regime between individual galaxies and massive clusters. Despite being the most common collapsed structures in the Universe, they remain among the least well characterised environments for dark matter studies. Strong gravitational lensing offers a uniquely direct, model-independent probe of their inner projected mass, yet confirmed group-scale strong lenses are rare and their analysis requires methodology that bridges the approaches used at galaxy and cluster scales.

This thesis presents a strong gravitational lensing analysis of the galaxy group ACO 3827 ($z = 0.099$), a quadruply-imaged system in which four massive early-type galaxies jointly lens a background source at $z_s = 1.24$. The analysis is implemented in Lenstronomy and follows a three-stage pipeline: parametric Sérsic modeling of the group galaxy light and intra-group light, conjugate-point optimisation of the lens mass using identifiable arc features as astrometric constraints, and full surface brightness reconstruction fitting the lens mass and source light simultaneously.

The group galaxy light is well described by elliptical Sérsic profiles with indices $n = 3.2$-6.9 and effective radii of $1.3''$-$3.2''$, consistent with massive early-type galaxies. A systematic comparison between single-galaxy and simultaneous four-galaxy fitting reveals a factor of ~ 1.8 discrepancy in the inferred intra-group light background level, quantifying a fundamental degeneracy between the intra-group light and the extended Sérsic wings of individual group members.

The conjugate-point mass model with four Singular Isothermal Ellipsoid profiles reproduces all conjugate groups with source-plane scatter well below 150 mas. Adding a group-scale halo as a fifth component reduces the mean scatter by $\approx 35\%$, providing clear evidence that the individual galaxy halos alone do not account for the full projected mass within the lensing region. This improvement is confirmed by the full surface brightness reconstruction, in which the halo is required to correctly reproduce the caustic geometry and the positions of peripheral star-forming knots in the source plane. The source is reconstructed as a spatially extended star-forming galaxy spanning ~ 8.5 kpc, consistent with a massive disk galaxy at cosmic noon. These results establish that a smooth, extended group-scale dark matter component is robustly required by the data, and lay the groundwork for a full dark matter fraction measurement pending multi-band stellar mass estimates from Spectral Energy Distribution fitting.

Acknowledgments

First, I would like to sincerely thank my supervisors, Guillaume Mahler and Dominique Sluse for introducing me to this topic and helping me reach the objectives of this work throughout the year. Their encouragement and insightful comments during our discussions have enabled me to work as efficiently as possible towards producing interesting results. Working on this subject was a good challenge for me as it is quite different from anything I had done during my Engineering degree. Without help from my supervisors, guiding me towards relevant lectures and topics, this would have been impossible.

I would also like to thank my family, particularly my parents and my two sisters, as I end this long stretch of my life through my years at university. You have taught me at least as much as I have learned during classes. I look forward to leading my life in the world as I finally become a functioning member of society.

To my friends, most of whom I made in the heat of battle at the University, I am so glad to have met you and will be cherishing your friendship for years to come. Robin, as always you have been present, even from the far-land of Austria, I know I can count on you anytime life gives me a hard time. Andrea, Nyota and Juliette, thank you for being amazing friends throughout the year and for your shoulders I could lean on when the mental load was a bit much. Finally Zoé, I know I can always count on you to pick me up when I fall, I look forward to our future as we embrace our respective dreams of working abroad.

This work concludes this year of studying the Space Sciences on a high note as it completes my curriculum that started in the Faculty of Engineering and now ends in the Faculty of Sciences with some very interesting research work. This helped me learn more about the job of a researcher and define a clearer path for my future post studies.

Contents

Acronyms

ΛCDM Lambda Cold Dark Matter. v, 1, 2, 4–9, 11–13, 23, 24, 26, 32, 33

2dFGRS 2-degree Field Galaxy Redshift Survey. 9

ACS/WFC Advanced Camera for Surveys. 39, 74

ACT Atacama Cosmology Telescope. 9, 12

AGN Active Galactic Nucleus. 5, 10, 12–14, 30

BCG Brightest Cluster Galaxy. 10, 11, 15, 67

BGG Brightest Group Galaxy. 10–12, 15, 21, 23, 26–30, 32–34, 36

CASSOWARY Cambridge And Sloan Survey Of Wide ARcs in the skY. 32, 33, 67, 74

CDM Cold Dark Matter. 5

CMB Cosmic Microwave Background. 5, 9

CSE Core-Softened Ellipsoid. 24, 47

eROSITA extended ROentgen Survey with an Imaging Telescope Array. 33

FITS Flexible Image Transport System. 40

GAMA Galaxy And Mass Assembly. 12

GL Gravitational Lensing. 15, 22

gNFW Generalised Navarro-Frenk-White. 7

GR General Relativity. 16

H I Neutral atomic Hydrogen. 10

HMF Halo Mass Function. 7, 8, 31, 73

HST Hubble Space Telescope. 2, 21, 30, 35, 37–41, 45, 67, 70, 73, 74

ICL Intra-Cluster Light. 68, 69

ICM Intracluster Medium. 9, 10, 12, 30

IGL Intra-Group Light. vi, 2, 35, 38, 39, 43, 44, 48, 50, 62, 63, 68–74

IGrM Intragroup Medium. 10–12, 28, 30, 31

JWST James Webb Space Telescope. 21, 33, 74

LSST Legacy Survey of Space and Time. 33, 74

MCMC Markov Chain Monte Carlo. 22

MSD Mass-Sheet Degeneracy. 25, 26, 70

MUSE Multi Unit Spectroscopic Explorer. 34

NFW Navarro-Frenk-White. vi, vii, 6, 7, 13, 21, 24–29, 32, 47, 50, 53–56, 59–61, 63–69, 72, 73

NIRCam Near Infrared Camera. 33

NISP Near Infrared Spectrometer and Photometer. 33

PIEMD Pseudo-Isothermal Elliptical Mass Distribution. 19, 20, 25

PSF Point Spread Function. 2, 23, 41, 66, 70

PSO Particle Swarm Optimization. vi, 42–44, 47–49, 53

rms Root Mean Square. 8, 63

SDSS Sloan Digital Sky Survey. 9, 11, 29, 32

SED Spectral Energy Distribution. 26, 28, 64, 69, 73

SHMR Stellar-to-Halo Mass Relation. 13, 14, 28–30, 64, 67, 73

SIDM Self-Interacting Dark Matter. 7

SIE Singular Isothermal Ellipsoid. vi, vii, 23, 24, 27, 28, 36, 45, 47, 48, 50, 53–61, 63–65, 67–69, 72

SL Strong Lensing. 18–21, 27, 30–33

SL2S Strong Lensing Legacy Survey. 32, 33, 67, 74

SNR Signal-to-Noise Ratio. 15, 22

SPT South Pole Telescope. 9, 11, 12

SZ Sunyaev-Zel'dovich. 9, 11–13

VIS Visible Imager. 33

VLT Very Large Telescope. 34

WDM Warm Dark Matter. 7

WFC3 Wide Field Camera 3. 39

WHIM Warm-Hot Intergalactic Medium. 12

WL Weak Lensing. 19

Chapter 1

Introduction

The formation and large-scale organisation of galaxies is one of the deepest open questions in modern astrophysics. Within the standard Lambda Cold Dark Matter (ΛCDM) cosmological framework, galaxies are not isolated objects: they are the luminous tracers of a pervasive dark matter distribution, assembled through billions of years of hierarchical merging and accretion. Dark matter constitutes approximately 27 % of the total energy budget of the Universe, yet its fundamental nature and spatial distribution on intermediate scales remain poorly constrained observationally.

The structures that make up the Universe span an enormous range of masses, from individual dwarf galaxies ($M \lesssim 10^9\,\mathrm{M}_\odot$) to massive galaxy clusters ($M \sim 10^{14}$-$10^{15}\,\mathrm{M}_\odot$). Galaxy groups occupy the critical intermediate regime, with total masses of 10^{13}-$10^{14}\,\mathrm{M}_\odot$, and represent the most common collapsed structures in the Universe: roughly half of all galaxies in the local Universe reside in group environments (Eke et al. [2004]). This places them in a distinct evolutionary niche from proto-clusters - overdense, yet gravitationally unbound large-scale structures destined to collapse into clusters at later epochs (Overzier [2016]) - which trace the high-redshift assembly of the cosmic web rather than representing virialised intermediate-mass halos. Galaxy groups are virialised collapsed objects, and as such they contribute to cluster growth through hierarchical merging and serve as sites of pre-processing of galaxy populations before cluster infall (Fujita [2004]). Despite their abundance and evolutionary importance, galaxy groups remain among the least well characterised mass scales in the dark matter hierarchy. At cluster scales, rich arc systems and thousands of background sources make strong gravitational lensing a mature tool; at galaxy scales, the Einstein-radius technique is applied to thousands of lens systems from wide-field surveys. Groups sit in between: their Einstein radii of $\theta_\mathrm{E} \sim 5$-$15''$ are too large for standard galaxy-lens analyses and too small to produce the spectacular arc systems of rich clusters, making confirmed group-scale strong lenses comparatively rare (e.g. Limousin et al. [2009]).

Gravitational lensing is the most direct probe of the total projected mass of any astrophysical system, requiring no assumptions about the dynamical or thermal state of the lens (Bartelmann & Schneider [2001]). Unlike X-ray hydrostatic mass estimates - which are subject to a systematic bias of 10-30 % from non-thermal pressure support (Pratt et al. [2019]) - or weak lensing stacking analyses that average over the structural diversity of group populations (Leauthaud et al. [2010]), strong gravitational lensing provides a per-system, model-independent measurement of the inner projected mass, directly sensitive to the dark matter halo and its decomposition from the stellar mass of the central group galaxy. At group scales, this makes strong lensing an exceptionally powerful and largely unexploited probe of intermediate-scale dark matter structures. This intermediate regime also presents a distinctive methodological challenge for lens modeling. At galaxy scales, galaxy-galaxy lensing is routinely addressed through pixellated source-reconstruction techniques, which model the full surface brightness distribution of the lensed emission. At cluster scales, the multiplicity and positional precision of strongly lensed images lend themselves to conjugate-point optimisation, where identified counter-image positions serve as astrometric constraints on the mass model. Galaxy groups sit precisely at the boundary where both approaches become simultaneously applicable and simultaneously challenged: the arc morphology is too complex and extended for simple positional modeling alone, yet the signal-to-noise and image multiplicity rarely reach the rich-cluster regime required for robust source reconstruction without strong regularisation. Developing methodology that bridges these two regimes is therefore a key open problem in group-scale lensing.

This thesis presents a strong gravitational lensing and multi-wavelength analysis of the galaxy group ACO 3827 ($z = 0.099$), a quadruply-imaged system with a well-resolved arc structure produced by four massive early-type galaxies acting as a joint lens for a background source at $z_s = 1.24$. ACO 3827 is one of a small number of group-scale strong lenses amenable to detailed individual analysis, and its proximity together with archival Hubble Space Telescope (HST) imaging makes it an ideal system for developing and testing group-scale lensing methodology. The analysis follows a three-stage pipeline: parametric modeling of the group galaxy light and Intra-Group Light (IGL), conjugate-point optimisation of the lens mass using the positions of identifiable arc features as astrometric constraints, and full surface brightness reconstruction combining lens light, lens mass, and source light simultaneously. The primary scientific goals are to establish whether a smooth group-scale dark matter halo is required beyond the individual galaxy halos, and to lay the groundwork for a full dark matter fraction measurement pending multi-band stellar mass estimates.

The thesis is structured as follows. Chapter 2 provides the theoretical background on galaxy formation, dark matter halos, and the properties of galaxy groups as intermediate-scale structures within the ΛCDM framework. Chapter 3 introduces the formalism of gravitational lensing, covering the lens equation, convergence and shear, mass modeling strategies, the dark matter fraction, and the current state of group-scale strong lensing studies. Chapter 4 describes the target system ACO 3827, its prior observations, group membership, lensing geometry, multi-band imaging, and intra-group light. Chapter 5 details the complete analysis pipeline, from data preparation and Point Spread Function (PSF) modeling through lens light fitting, conjugate-point mass optimisation, and full surface brightness modeling. Chapter 6 presents the results of each pipeline stage. Chapter 7 interprets these results in the context of the dark matter halo properties of ACO 3827, the intermediate mass scale, and the principal systematic uncertainties. Chapter 8 summarises the conclusions and outlines directions for future work.

Chapter 2

Galaxy Formation

The formation and evolution of galaxies represents one of the most complex and multi-faceted problems in modern astrophysics. Galaxies are not isolated objects; they are the luminous tracers of an underlying dark matter distribution, shaped by a rich interplay of gravitational collapse, hydrodynamical processes, and feedback mechanisms operating across a vast range of physical scales. Understanding how galaxies form and evolve is therefore deeply intertwined with understanding the nature and distribution of dark matter itself.

The modern picture of galaxy formation is rooted in the Lambda Cold Dark Matter (ΛCDM) cosmological model, in which the Universe is dominated by cold dark matter and a cosmological constant Λ (Blumenthal et al. [1984]). Within this framework, small perturbations in the primordial density field grow through gravitational instability over cosmic time, causing overdense regions to collapse and form dark matter haloes - the fundamental building blocks of cosmic structure (Press & Schechter [1974]; White & Rees [1978]). Baryonic matter[1] falls into the gravitational potential wells of these haloes, cools, and eventually forms stars, giving rise to the galaxies we observe today (Rees & Ostriker [1977]).

Galaxy formation in ΛCDM proceeds hierarchically: small structures form first and progressively merge to form more massive systems over time (White & Frenk [1991]). This picture is well-supported by N-body simulations (Springel et al. [2005]) and observations of the large-scale structure of the Universe (Davis et al. [1985]; Alam et al. [2017]). On the largest scales, dark matter is distributed across a network of filaments, sheets, and voids known as the *cosmic web* (Bond et al. [1996]), with galaxy groups and clusters residing at the densest intersections of this structure.

Galaxy groups occupy an intermediate mass regime between individual galaxies and massive clusters, with total masses in the range 10^{13}-10^{14} $M_{\odot}$ (Kravtsov & Borgani [2012]). These systems are particularly valuable for studying dark matter, as they are massive enough to retain a significant dark matter halo while remaining numerous enough to provide statistically meaningful samples. The properties of galaxies - their morphology, stellar mass, and star formation rate

[1] "Ordinary" matter composed of baryons (protons and neutrons) by opposition to dark matter.

- are closely linked to those of their host dark matter haloes (Behroozi et al. [2013]), with feedback processes from supernovae and Active Galactic Nucleus (AGN) playing a key role in regulating star formation across different mass scales (Croton et al. [2006]).

Despite the broad success of ΛCDM, several tensions remain on small scales, including discrepancies in the number of low-mass satellite galaxies and in the predicted inner density profiles of dark matter haloes (Boylan-Kolchin et al. [2011]; Pontzen & Governato [2012]; Bullock & Boylan-Kolchin [2017]). These open questions motivate detailed observational studies of dark matter structure across a range of mass scales, from individual galaxies to groups and clusters.

This chapter provides the theoretical background necessary to contextualise the subsequent analysis. The following sections discuss the formation and properties of dark matter haloes (Section 2.1), the large-scale structures and the role of the cosmic web (Section 2.2), and the specific properties of galaxy groups as intermediate-scale structures (Section 2.3).

2.1 Dark Matter

Dark matter constitutes the dominant mass component of the Universe, yet its fundamental nature remains unknown. In the ΛCDM framework, dark matter is cold, collisionless, and interacts only gravitationally with baryonic matter. This section reviews the cosmological context in which dark matter operates, the observational evidence that established its existence, the theoretical models describing how it is distributed within haloes, and the tensions that persist on small scales.

2.1.1 The ΛCDM model

The standard cosmological model, ΛCDM, describes a spatially flat universe whose energy budget is dominated by a cosmological constant Λ (associated with dark energy, $\sim 68\%$) and Cold Dark Matter (CDM) ($\sim 27\%$), with baryonic matter accounting for only $\sim 5\%$ (Planck Collaboration et al. [2020]). The Cosmic Microwave Background (CMB) anisotropy spectrum measured by the *Planck* satellite provides the most precise constraints on these parameters to date (Planck Collaboration et al. [2020]). Within this framework, the primordial density field is seeded by quantum fluctuations during inflation, described by a nearly scale-invariant power spectrum (Peebles [1982]). These perturbations grow through gravitational instability, with dark matter - which decouples from radiation early and is not subject to radiation pressure - beginning to cluster before baryons (Blumenthal et al. [1984]). Structure formation therefore proceeds hierarchically, with small haloes forming first and merging progressively into larger systems (Press & Schechter [1974]).

The success of ΛCDM in reproducing the large-scale structure of the Universe - from the CMB power spectrum to the distribution of galaxies - makes it the foundation upon which all modern models of galaxy formation are built (Davis et al. [1985]; Springel et al. [2005]).

2.1.2 Observational evidence

Evidence for dark matter spans an enormous range of physical scales and has accumulated from multiple independent observational probes.

On galactic scales, the rotation curves of spiral galaxies provided the first compelling evidence that light does not trace mass. Stars and gas at large radii orbit at velocities far in excess of what the visible baryonic mass would predict, implying the existence of an extended mass distribution - the dark matter halo (Rubin et al. [1980]). This result, originally obtained for a sample of spiral galaxies, has since been confirmed in hundreds of systems across a wide range of masses.

On the scales of galaxy groups and clusters, the mass of the hot intracluster gas, measured through its X-ray emission, falls far short of the dynamical mass inferred from galaxy velocities or from gravitational lensing (Kravtsov & Borgani [2012]). The *Bullet Cluster* provides a particularly striking illustration: the spatial offset between the X-ray emitting gas - which was slowed by ram pressure during a cluster merger - and the total mass distribution reconstructed from weak gravitational lensing demonstrates that the dominant mass component is collisionless, as expected for dark matter (Clowe et al. [2006]).

2.1.3 Halo density profiles

The internal structure of dark matter haloes is a key prediction of ΛCDM that can be tested against observations. *N*-body simulations of collisionless dark matter have shown that haloes formed through hierarchical merging share a universal density profile, regardless of mass or cosmological epoch (Navarro et al. [1996]).

The most widely used parametrisation is the Navarro-Frenk-White (NFW) profile, introduced by Navarro et al. [1996], which takes the form:

$$\rho(r) = \frac{\rho_s}{(r/r_s)(1 + r/r_s)^2}, \tag{2.1}$$

where ρ_s is a characteristic density and r_s is the scale radius at which the logarithmic slope of the profile equals -2. The profile scales as $\rho \propto r^{-1}$ in the centre (a cusp) and as $\rho \propto r^{-3}$ in the outer regions, transitioning at r_s. The concentration parameter $c = r_{200}/r_s$, where r_{200} is the radius enclosing a mean density 200 times the critical density, characterises the compactness of the halo.

An alternative profile proposed by Moore et al. [1999] predicts a steeper central slope ($\rho \propto r^{-1.5}$), also referred to as a cusp, though steeper than the NFW prediction. Both profiles contrast with observational evidence in low-mass galaxies that often favours a central density core ($\rho \sim$ const) rather than a cusp - a discrepancy discussed further in Section 2.1.4.

More generally, halo profiles are characterised by their slope γ in the inner regions and are often described using the generalised Hernquist form or the Generalised Navarro-Frenk-White (gNFW) profile:

$$\rho(r) = \frac{\rho_s}{(r/r_s)^\gamma (1 + r/r_s)^{3-\gamma}}, \tag{2.2}$$

which reduces to the NFW profile for $\gamma = 1$. Gravitational lensing provides one of the most direct and model-independent means of constraining these profiles across a range of mass scales (Monna et al. [2014]), making it a central tool in the analysis presented in this work.

2.1.4 Group-scale tensions

Despite its broad success, ΛCDM faces a number of persistent challenges on small scales - the very scales that galaxy groups probe most directly.

The *core-cusp problem* refers to the discrepancy between the cuspy inner density profiles predicted by dark-matter-only simulations (Navarro et al. [1996]; Moore et al. [1999]) and the cored profiles inferred observationally in dwarf and low-surface-brightness galaxies. Baryonic feedback processes - particularly supernova-driven outflows that repeatedly expel gas from the centre of a halo - can in principle flatten cuspy profiles into cores (Pontzen & Governato [2012]), though the extent to which this operates across different mass scales remains debated.

The *missing satellites problem* describes the large discrepancy between the number of low-mass subhaloes predicted by N-body simulations and the observed population of dwarf satellite galaxies around the Milky Way (Moore et al. [1999]). Proposed solutions include suppression of star formation in low-mass haloes by reionisation feedback and tidal disruption, though the tension has not been fully resolved.

The *too-big-to-fail problem* notes that the most massive subhaloes predicted by simulations are too dense to host any of the observed bright satellites of the Milky Way (Boylan-Kolchin et al. [2011]). This problem also arises in field dwarfs and in the satellites of other galaxies, suggesting it may not be an artifact of the Milky Way's specific environment.

These tensions have motivated alternative dark matter models - including Warm Dark Matter (WDM), Self-Interacting Dark Matter (SIDM), and fuzzy dark matter - as well as more sophisticated baryonic feedback prescriptions. The degree to which these tensions persist in intermediate-mass systems such as galaxy groups, where both simulations and observations are less well-constrained than for clusters or individual galaxies, remains an open question and is one of the primary motivations for the work presented in this work.

2.1.5 The Halo Mass Function

The Halo Mass Function (HMF) describes the comoving number density of dark matter haloes per unit mass interval, $\mathrm{d}n/\mathrm{d}M$, and is one of the most powerful statistical predictions of the ΛCDM framework. It encodes how structure formation proceeds across mass scales and provides a direct link between the underlying cosmology and the observed population of collapsed objects.

The foundational analytical framework was established by Press & Schechter [1974], who derived the HMF assuming spherical collapse of perturbations in a Gaussian density field. This formalism predicts a power-law rise in halo abundance toward low masses and an exponential suppression above a characteristic mass M^*, set by the scale at which the Root Mean Square (rms) density fluctuations $\sigma(M)$ equal the collapse threshold δ_c. Extensions to the original Press & Schechter [1974] model - collectively referred to as Extended Press-Schechter theory - account for ellipsoidal collapse and environmental effects, improving agreement with simulations at both ends of the mass spectrum.

Modern calibrations of the HMF rely on large N-body simulations (Springel et al. [2005]), which have produced fitting functions accurate to $\sim 5\%$ over a wide range of masses and redshifts (Tinker et al. [2008]). The shape and normalisation of the HMF are sensitive to cosmological parameters: the amplitude of matter fluctuations σ_8 sets the overall normalisation, while the matter density Ω_m shifts the location of the exponential cutoff mass M^*.

Galaxy groups, with halo masses in the range 10^{13}-$10^{14}\,M_\odot$ (Kravtsov & Borgani [2012]), occupy the transition regime between the power-law and exponential parts of the HMF. This makes them particularly sensitive to cosmological parameters and hence valuable as a cosmological probe: the observed abundance of groups and clusters as a function of mass and redshift can be compared directly to HMF predictions to constrain σ_8 and Ω_m (Planck Collaboration et al. [2020]).

2.2 Large-Scale Structure and the Cosmic Web

The distribution of matter in the Universe is far from uniform. On the largest scales, galaxies and their host haloes are not isolated objects but are instead embedded within a complex network of structures whose geometry and dynamics are shaped by the gravitational amplification of primordial density perturbations. This large-scale environment plays a fundamental role in determining how galaxies form and evolve, and it provides the broader context within which galaxy groups and clusters assemble. This section describes the organisation of matter across cosmic scales, introducing the structural components of the cosmic web, the properties of galaxy clusters, and the key environmental mechanisms that drive galaxy evolution in dense environments.

2.2.1 The Cosmic Web

The ΛCDM model predicts that the gravitational collapse of small primordial density fluctuations gives rise to a web-like distribution of matter on large scales (Bond et al. [1996]). In its early stages, this collapse proceeds anisotropically:

the Zel'dovich approximation describes how overdense regions first flatten into sheets, then contract into elongated filaments, and finally collapse into compact nodes (Davis et al. [1985]). The result is the *cosmic web*, a hierarchical network of interconnected structures organised by the local geometry of the density and tidal fields.

Four broad structural components are typically identified. *Filaments* are elongated, overdense structures that connect the densest nodes of the web; they act as the primary channels through which matter, gas, and galaxies are channeled toward group and cluster haloes over cosmic time. *Sheets* (or walls) are flattened structures of intermediate density that bound the underdense regions. *Voids* are the large, expanding underdense regions that occupy roughly 80% of the volume of the Universe; they host relatively few, predominantly blue, star-forming galaxies. Finally, *nodes* mark the densest intersections of filaments and are the preferred sites of group and cluster formation.

This predicted topology has been confirmed observationally through large galaxy redshift surveys such as the 2-degree Field Galaxy Redshift Survey (2dFGRS) and the Sloan Digital Sky Survey (SDSS), which reproduce the filamentary structure seen in ΛCDM N-body simulations (Springel et al. [2005]). Within this framework, galaxy groups and clusters reside at the nodes of the cosmic web, and their assembly history and mass accretion rate are partly governed by the surrounding large-scale tidal field and the rate of filamentary infall.

2.2.2 Galaxy Clusters

Galaxy clusters are some of the most massive gravitationally bound structures in the Universe, with halo masses of $M \sim 10^{14}$-$10^{15}\,M_\odot$ and memberships ranging from hundreds to thousands of galaxies (Kravtsov & Borgani [2012]). They form at the densest nodes of the cosmic web through the hierarchical merging of smaller structures.

Clusters are multi-component systems observable across the electromagnetic spectrum. Their most massive baryonic constituent is the Intracluster Medium (ICM), a hot plasma enriched by supernova ejecta and maintained at temperatures of $T \sim$ 4-10 keV. At these temperatures, the gas emits abundantly in X-rays through thermal bremsstrahlung - radiation produced by decelerating free electrons - making clusters among the brightest X-ray sources in the sky, as observed by *Chandra* and *XMM-Newton*. The ICM can also be detected through the Sunyaev-Zel'dovich (SZ) effect, whereby ICM electrons scatter CMB photons to higher energies, leaving a characteristic spectral distortion exploited by several observatories like *Planck*, the South Pole Telescope (SPT), or the Atacama Cosmology Telescope (ACT).

Beyond the hot gas, the kinematics of member galaxies - which exhibit velocity dispersions of $\sigma \sim$ 500-1500 km s^{-1} - independently trace the depth of the gravitational potential, and the cluster mass distribution frequently shows rich substructure from merging subclusters, infalling groups, and filamentary accretion (Kravtsov & Borgani [2012]). The most luminous member is typically the

Brightest Cluster Galaxy (BCG), a giant elliptical galaxy sitting near the potential minimum and grown primarily through mergers and the gradual accretion of satellite galaxies.

Owing to their large masses, clusters are the most efficient gravitational lenses in the Universe, producing strong lensing features such as arcs and multiple images of background sources, which are discussed in detail in Chapter 3. Their abundance as a function of mass and redshift is highly sensitive to the cosmological parameters, making clusters among the most powerful probes of dark energy (Planck Collaboration et al. [2020]).

2.2.3 Environmental Effects on Galaxy Evolution

Galaxy properties - including colour, morphology, star formation rate, and gas content - correlate strongly with environment, independently of halo mass (Dressler [1980]). Disentangling the internal, mass-driven processes from externally driven, environment-induced quenching remains one of the central challenges of galaxy formation theory. The morphology-density relation, first established by Dressler [1980], illustrates this clearly: elliptical and quenched galaxies are preferentially found in dense nodes, while star-forming spirals dominate in filaments and voids.

Several physical mechanisms operate specifically in group and cluster environments to suppress star formation in satellite galaxies. *Ram pressure stripping* occurs when the hot Intragroup Medium (IGrM) or ICM exerts a drag force on infalling satellites, rapidly removing their cold interstellar gas; this process is most efficient in dense cores and can be directly imaged in nearby systems (Boselli et al. [2022]). *Strangulation* (or starvation) refers to the removal of the diffuse hot gas reservoir surrounding a satellite, cutting off its future supply of cold gas and quenching star formation on longer timescales. *Tidal interactions and harassment* - gravitational distortions from the group potential and high-speed galaxy-galaxy encounters - can trigger starbursts or drive gas toward the nucleus, potentially fuelling AGN activity in the Brightest Group Galaxy (BGG). Finally, *mergers* are more frequent in groups than in clusters due to their lower velocity dispersions, and they can drive significant morphological transformation (Barnes & Hernquist [1992]).

An important consequence of group-scale processing is *pre-processing*: galaxies may be substantially quenched within group-scale haloes before they are accreted onto a more massive cluster (Fujita [2004]). This has direct implications for the interpretation of cluster galaxy populations and highlights the role of groups as an intermediate evolutionary stage. Observational signatures of environmental quenching - an elevated red fraction, Neutral atomic Hydrogen (H I) deficiency, and suppressed star formation rate - are all observed to increase toward the centres of groups and clusters, confirming the importance of these mechanisms across the full range of halo masses studied in this work.

2.3 Galaxy Groups

Galaxy groups are the most common collapsed structures in the Universe, representing the typical environment for approximately half of all galaxies out to at least $z \sim 0.5$ (Eke et al. [2004]; Robotham et al. [2011]; Lovisari et al. [2021]). They occupy an intermediate mass regime between individual galaxies and massive clusters, with total masses in the range 10^{13}-$10^{14}\,\mathrm{M}_\odot$, making them sensitive probes of both baryonic and dark matter physics. Groups are also the direct progenitors of clusters via hierarchical merging (Kravtsov & Borgani [2012]), and are the dominant sites of pre-processing of galaxy populations before cluster infall (Fujita [2004]).

2.3.1 Definition and Observational Identification

Galaxy groups are conventionally defined as systems with total masses in the range $M \sim 10^{13}$-$10^{14}\,\mathrm{M}_\odot$, hosting between approximately 3 and 50 member galaxies. The distinction between groups and clusters is conventional rather than physical, and reflects a continuum of halo masses in ΛCDM. Throughout this work, the standard mass definition M_{200} is adopted, corresponding to the total mass enclosed within the virial radius r_{200}, defined as the radius within which the mean enclosed density equals 200 times the critical density of the Universe.

Observationally, groups are characterised by X-ray temperatures $T_X \sim 0.5$-$2\,\mathrm{keV}$ (compared to $> 2\,\mathrm{keV}$ for clusters), and galaxy velocity dispersions $\sigma \sim$ 200-500 $\mathrm{km\,s^{-1}}$ (compared to 500-1500 $\mathrm{km\,s^{-1}}$ for clusters). Their lower X-ray surface brightness makes detection more challenging than for massive clusters. The dominant member galaxy, the BGG, typically sits near the potential minimum and dominates the optical luminosity, in analogy with the BCG in clusters but formed in a lower-mass environment.

Several complementary observational methods are used to identify and characterise galaxy groups. In the optical, richness estimators and photometric redshifts are commonly used, though these are subject to projection effects and line-of-sight contamination, while spectroscopic redshifts provide more reliable membership determination. X-ray observations reveal the extended emission from the hot IGrM, with luminosity and temperature serving as mass proxies; however, groups are harder to detect than clusters owing to their lower surface brightness. The SZ effect provides a signal that scales with thermal energy ($Y_{\mathrm{SZ}} \propto M$) and is less biased by cool cores than X-ray emission; it is increasingly accessible at group scales with current and upcoming instruments such as SPT-3G and the Simons Observatory. Finally, weak gravitational lensing provides a direct projected mass measurement, though the signal-to-noise per system at group scales is low, typically requiring stacking over large statistical samples (Leauthaud et al. [2010]).

Major group catalogues include X-ray selected samples based on *eROSITA*, optically selected catalogues from SDSS-based friends-of-friends algorithms and the Galaxy And Mass Assembly (GAMA) survey, and SZ-selected samples from *Planck*, SPT, and ACT.

2.3.2 Baryonic Content

The baryonic content of galaxy groups is distributed between the hot IGrM, the stellar mass of member galaxies, and a substantial reservoir of warm-hot gas that remains undetected in current surveys. The IGrM is an X-ray emitting plasma at temperatures $T \sim 0.5\text{-}2\,\text{keV}$, with lower metallicity than the ICM of massive clusters. Its X-ray emissivity scales steeply with temperature (observed slopes of $L_X \propto T^{3\text{-}5}$ at group scales, compared to the self-similar prediction of $L_X \propto T^2$; Lovisari et al. [2015]; Helsdon & Ponman [2000]), making detection and modeling more difficult at the low-mass end.

Some groups exhibit a short central cooling time and a temperature drop towards the centre, constituting a cool core, while others are isothermal or dynamically disturbed (non-cool core). This dichotomy has implications for X-ray mass modeling and AGN activity level. The gas fraction in groups is systematically lower than in clusters, with f_{gas} increasing roughly as $M^{0.3}$ (Sun et al. [2009]); this deviation from self-similar scaling is driven by AGN and supernova feedback, which eject gas beyond the virial radius preferentially in lower-mass systems. A significant fraction of group baryons is therefore expected to reside in the warm-hot intergalactic medium (Warm-Hot Intergalactic Medium (WHIM), $T \sim 10^5\text{-}10^7\,\text{K}$), which remains undetected in X-ray emission.

The stellar mass budget is dominated by the BGG, with the satellite contribution declining steeply with group mass. Most group members are quenched and occupy the red sequence, the result of environment-driven quenching through ram pressure stripping, strangulation, and tidal interactions (Boselli et al. [2022]). AGN feedback from the BGG suppresses cooling flows, regulates star formation, and drives gas outflows that redistribute baryons - potentially affecting the inner dark matter profile by reducing the baryonic contribution to the central gravitational potential (Croton et al. [2006]).

2.3.3 Dark Matter in Galaxy Groups

Galaxy groups are among the most dark-matter-dominated environments accessible to detailed observational study, with mass-to-light ratios peaking at group scales in the range $\sim 100\text{-}300\,\text{M}_\odot/\text{L}_\odot$. The total mass decomposition of a group requires disentangling contributions from the dark matter halo, the BGG stellar mass, satellite galaxies, and the IGrM; this is most robustly achieved through multi-probe analyses combining lensing, X-ray, and dynamical constraints.

In ΛCDM, the concentration-mass relation predicts that halo concentration c decreases with increasing halo mass (Navarro et al. [1996]). Groups occupy an intermediate concentration range ($c \sim 4\text{-}8$), between galaxy-scale haloes ($c \sim 10\text{-}20$) and massive clusters. Observational constraints at group scales remain uncertain due to degeneracies in mass modeling and the limited number of well-studied systems. The inner profile slope is particularly poorly constrained at group scales: groups sit between well-studied dwarf galaxies - where dark matter cores are often observed [Pontzen & Governato, 2012] - and clusters, where NFW cusps are broadly consistent with observations [Newman et al., 2013]. Whether groups host cusps or cores remains an open question, and one that the analysis presented in this work aims to address.

Baryonic contraction - the steepening of the inner dark matter profile in response to baryonic infall - can modify the expected NFW shape at the centre (Blumenthal et al. [1986]). However, AGN-driven outflows can partially or fully counteract this effect; the net outcome at group scales remains uncertain and highly model-dependent. Groups also host subhaloes associated with satellite galaxies, whose mass function and disruption rates provide additional tests of ΛCDM predictions on these intermediate scales.

Several observational methods are used to constrain the dark matter distribution in groups. X-ray mass modeling assumes hydrostatic equilibrium, introducing a hydrostatic mass bias discussed in detail in Section 2.3.4. Velocity dispersions rely on the assumption of dynamical equilibrium and are sensitive to membership contamination. Weak gravitational lensing and strong gravitational lensing complement these methods by providing direct projected mass measurements independent of the thermal or dynamical state of the system, as introduced in Section 2.3.1. Strong lensing in particular directly constrains the inner mass profile and, while rare at group scales, is highly informative when available [Monna et al., 2014]. Gravitational lensing is therefore the primary observational tool used in this work and is introduced in detail in the following chapter.

2.3.4 Scaling Relations

Scaling relations between observable proxies and total halo mass are essential tools for group cosmology, enabling mass calibration across large samples. The key relations include the X-ray luminosity-mass (L_X-M), temperature-mass (T_X-M), velocity dispersion-mass (σ-M), SZ signal-mass (Y_{SZ}-M), richness-mass, and stellar-to-halo mass (Stellar-to-Halo Mass Relation (SHMR)) relations (Kravtsov & Borgani [2012]).

Under the assumption of pure gravitational collapse (self-similar scaling), simple virial and bremsstrahlung arguments yield $L_X \propto M^{4/3}$ and $T_X \propto M^{2/3}$. In practice, the observed slopes are steeper than these self-similar predictions at group scales, because baryonic feedback preferentially removes gas from lower-mass systems, suppressing their X-ray luminosity and reducing their gas fraction (Sun et al. [2009]). The intrinsic scatter in scaling relations is also larger in groups than in clusters, amplified by projection effects, varying dynamical states, and stronger sensitivity to feedback.

A further systematic affecting X-ray mass estimates is the hydrostatic mass bias: masses derived under the assumption of hydrostatic equilibrium underestimate the true (lensing) mass by $\sim$ 10-30% due to non-thermal pressure support from turbulence and bulk motions (Pratt et al. [2019]). This bias is larger in dynamically disturbed systems and is more uncertain at group than cluster scales.

The SHMR peaks at a halo mass of $M_{\rm halo} \sim 10^{12}\,{\rm M}_{\odot}$ (corresponding to L^{*} galaxies), and declines towards group scales (Behroozi et al. [2013]), implying a decreasing star formation efficiency with halo mass above the peak, driven by AGN feedback. Accurate calibration of scaling relations is required to use groups as cosmological probes; lensing-based mass calibration is the most robust approach and is a key application of the analysis presented in this work.

Chapter 3

Gravitational Lensing

Mapping the mass distribution of the Universe is one of the central challenges of modern astrophysics, and Gravitational Lensing (GL) stands out as the most direct observational tool available for this purpose. Unlike mass estimates based on X-ray emission or stellar dynamics, gravitational lensing is entirely model-independent in the sense that it requires no assumption about the dynamical or thermal state of the system: it responds directly to the total projected gravitational potential, irrespective of whether the mass is baryonic or dark (Bartelmann & Schneider [2001]). This makes it uniquely powerful in a context where alternative probes are known to be biased or limited.

As discussed in Chapter 2, galaxy groups occupy a transitional mass regime that is particularly challenging for mass characterisation. X-ray hydrostatic mass estimates suffer from a systematic hydrostatic bias at the level of 10-30 %, driven by residual non-thermal pressure support and gas bulk motions (2.3.4; Pratt et al. [2019]). In the weak-lensing regime (presented in section 3.2), the low Signal-to-Noise Ratio (SNR) per individual group system forces stacking analyses that wash out system-to-system structural diversity (2.3.1; Leauthaud et al. [2010]). Strong gravitational lensing, although rare at group scales, provides an exceptional and highly informative window into the innermost projected mass distribution of these intermediate-scale structures, including the contribution of the BCG or BGG and the dark matter halo in which it resides (2.3.3; Limousin et al. [2009]).

This chapter introduces the theoretical and observational framework for gravitational lensing that underpins the analysis presented in this thesis. Section 3.1 develops the lensing formalism from first principles, defining the deflection angle, convergence, shear, and magnification. Section 3.2 describes the observational signatures that distinguish the strong and weak lensing regimes and the specific observables exploited in each case. The mass modeling strategy adopted in this work is presented in Section 3.3, while Section 3.4 discusses the reconstruction of the radial mass profile and its decomposition into baryonic and dark matter components. Section 3.5 focuses on the dark matter fraction and what lensing can reveal about it at group scales. Finally, Section 3.6 reviews the current state of the art in strong lensing studies of galaxy groups, situating this thesis within the broader observational landscape.

3.1 Lensing Formalism

The theoretical framework of gravitational lensing rests on a small set of geometric and physical ingredients that can be assembled from first principles. This section builds that framework systematically, starting from the deflection of light in General Relativity (GR) and the thin lens approximation (3.1.1), then deriving the lens equation that maps image positions to source positions (3.1.2). The Einstein radius is introduced as the natural scale of the problem and as a direct mass estimator (3.1.3), before the local distortion properties of the lens mapping are described through the convergence, shear, and lensing Jacobian (3.1.4). Together, these quantities form the complete set of observables and derived quantities used throughout the analysis presented in this thesis.

3.1.1 Physical Basis: Light Deflection in General Relativity

The deflection of light by a gravitational potential is a fundamental prediction of GR. For a point mass M, the deflection angle is given by

$$\hat{\alpha} = \frac{4GM}{c^2 \xi}, \tag{3.1}$$

where ξ is the impact parameter. This result is exactly twice the Newtonian prediction and was confirmed observationally by Eddington during the 1919 solar eclipse, providing one of the earliest empirical validations of GR (Bartelmann & Schneider [2001]).

For extended mass distributions, the deflection angle generalises to a two-dimensional integral over the projected mass distribution along the line of sight, weighted by the impact parameter of each mass element relative to the light ray. This generalisation is made tractable by the thin lens approximation: all deflecting mass is assumed to be concentrated in a single plane perpendicular to the line of sight, the lens plane. This approximation is valid when the physical extent of the lens along the line of sight is much smaller than both the observer-lens and lens-source distances, a condition well satisfied for galaxy groups at cosmological distances (Bartelmann & Schneider [2001]).

The lensing potential $\psi(\theta)$ is defined as the two-dimensional projected Newtonian potential, rescaled by the ratio of distances $D_{LS}/(D_L D_S)$ (see 3.1.3 for the definition of these distances). All lensing observables follow as derivatives of ψ: the reduced deflection angle as its gradient ($\alpha = \nabla_\theta \psi$), the convergence as half its Laplacian ($\kappa = \frac{1}{2}\nabla^2\psi$), and the shear components from the traceless part of the Hessian ($\gamma_1 = \frac{1}{2}(\psi_{,11} - \psi_{,22})$, $\gamma_2 = \psi_{,12}$). The introduction of ψ renders the subsequent formalism self-contained and unambiguous.

3.1.2 The Lens Equation

The geometry of a lensing configuration involves three characteristic planes: the observer at $D = 0$, the lens plane at angular diameter distance D_L, and the source plane at angular diameter distance D_S, with a cross-plane distance D_{LS} between them, as illustrated in Fig. 3.1.

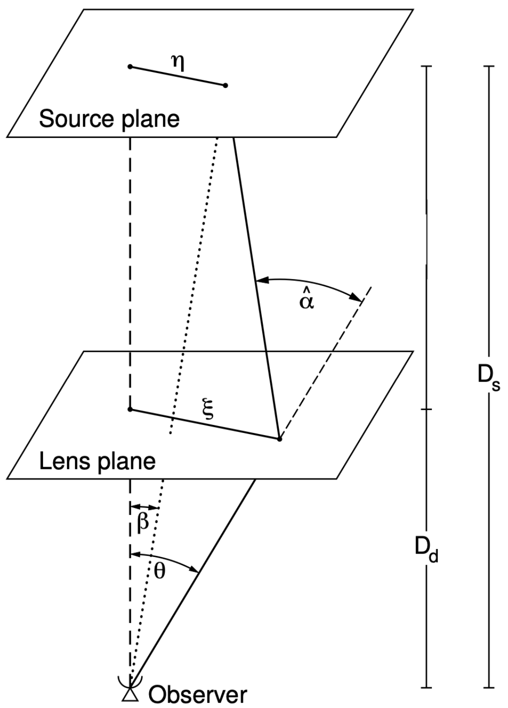

Figure 3.1: Geometry of the gravitational lensing configuration. The observer is at $D = 0$, the deflecting mass (lens) lies at angular diameter distance D_L, and the source is at D_S. The cross-plane distance D_{LS} enters the lens equation and determines the lensing efficiency. (Credits: Bartelmann & Schneider [2001])

In the thin lens approximation, the mapping between the observed image position θ and the true source position β is described by the lens equation:

$$\beta = \theta - \alpha(\theta), \tag{3.2}$$

where $\alpha = \nabla_\theta \psi$ is the reduced deflection angle (Bartelmann & Schneider [2001]). The physical deflection angle $\hat{\alpha}$ is related to the reduced one by $\alpha = (D_{LS}/D_S)\hat{\alpha}$.

A key feature of Eq. (3.2) is its potential multi-valuedness: a single source position β can correspond to multiple image positions θ when the lens is sufficiently massive. This multi-valuedness is the defining topological feature of the strong lensing regime and is ultimately responsible for the formation of multiple images and gravitational arcs.

3.1.3 Einstein Radius

The Einstein radius θ_E is the image radius produced when source, lens, and observer are in perfect alignment. For a circularly symmetric lens, it is defined by

$$\theta_E = \sqrt{\frac{4GM(<\theta_E)}{c^2} \frac{D_{LS}}{D_L D_S}}, \tag{3.3}$$

where $M(<\theta_E)$ is the projected mass enclosed within θ_E (Bartelmann & Schneider [2001]). Physically, the Einstein radius directly encloses the projected mass $M(<\theta_E) = \pi\theta_E^2 \Sigma_{\rm cr} D_L^2$, making it one of the most robust and assumption-free mass estimators in astrophysics: it depends only on geometry and the total projected mass, with no requirement on the dynamical or thermal state of the lens.

At group scales, typical Einstein radii lie in the range $\theta_E \sim$ 5-15$''$, intermediate between $\sim$ 1-3$''$ for galaxy-scale lenses and $\sim$ 30-60$''$ for massive clusters (Monna et al. [2014]). This intermediate size directly reflects the intermediate halo mass and explains both the observational challenges (Einstein radii comparable to the angular size of member galaxies, making arc detection and lens light subtraction significantly more complex than for cluster-scale systems) and the scientific value (access to the inner projected mass structure) of group-scale Strong Lensing (SL).

3.1.4 Convergence, Shear, and the Lensing Jacobian

The local properties of the lens mapping are encoded in the Jacobian matrix $\mathcal{A} = \partial\beta/\partial\theta$, which linearly maps an infinitesimal source element to the corresponding image element. It can be decomposed into two physically distinct contributions.

Convergence κ describes isotropic focusing. Physically, κ measures how much mass along the line of sight focuses light isotropically, uniformly rescaling the apparent size of a source.

Shear γ describes anisotropic distortion. Its two components, $\gamma_1 = \frac{1}{2}(\psi_{,11} - \psi_{,22})$ and $\gamma_2 = \psi_{,12}$, arise from the traceless part of the Hessian of ψ, and encode the tidal field of the projected mass distribution. Shear stretches images tangentially or radially depending on the local mass geometry, producing the characteristic arc shapes observed in SL (Bartelmann & Schneider [2001]).

The Jacobian matrix is written explicitly as

$$\mathcal{A} = (1-\kappa)\begin{pmatrix} 1 & 0 \\ 0 & 1 \end{pmatrix} - \begin{pmatrix} \gamma_1 & \gamma_2 \\ \gamma_2 & -\gamma_1 \end{pmatrix}, \tag{3.4}$$

with eigenvalues $(1-\kappa-|\gamma|)$ and $(1-\kappa+|\gamma|)$, corresponding to the tangential and radial magnification factors respectively. The magnification is then

$$\mu = \frac{1}{\det \mathcal{A}} = \frac{1}{(1-\kappa)^2 - |\gamma|^2}, \tag{3.5}$$

which diverges wherever $\det \mathcal{A} = 0$.

Critical curves are the loci in the image plane where $\det \mathcal{A} = 0$ and the magnification formally diverges. Their images in the source plane under the lens mapping are called caustics. Two topologically distinct types arise in typical lens models. Fold caustics are smooth curve segments; a source crossing a fold caustic gains or loses a pair of images of opposite parity, each appearing as a highly elongated tangential arc near the corresponding critical curve. Cusp caustics are singular points on the caustic network where three images merge; a source near a cusp produces a characteristic triplet of images, two of which form a bright arc. In practice, the tangential critical curve, where the tangential eigenvalue $(1 - \kappa - |\gamma|)$ vanishes, is the most prominent feature and encloses the Einstein radius for circularly symmetric lenses. The corresponding tangential caustic degenerates to a point for perfectly circular symmetry but opens into an extended curve for elliptical or irregular mass distributions. The structure of the caustic network therefore encodes directly the shape and substructure of the projected mass distribution, making it a powerful diagnostic tool for lens modeling (Bartelmann & Schneider [2001]), as illustrated for a Pseudo-Isothermal Elliptical Mass Distribution (PIEMD) in Fig. 3.2.

3.2 Strong and Weak Lensing: Regimes and Observables

The lensing formalism developed in Section 3.1 - convergence κ, shear γ, magnification μ, and the critical curves where $\det \mathcal{A} = 0$ - provides the theoretical foundation for understanding what is actually observed. In practice, the observational consequences of lensing depend strongly on the local values of κ and $|\gamma|$: whether one is working in the weak regime, where distortions are subtle, or the strong regime, where multiple discrete images and arcs are produced. This section focuses on the strong lensing regime and its characteristic observables, with weak lensing mentioned briefly for context.

3.2.1 The Weak and Strong Lensing Regimes

The distinction between Weak Lensing (WL) and Strong Lensing (SL) is not a binary classification but a continuum governed by the local amplitude of κ and $|\gamma|$ (Bartelmann & Schneider [2001]).

In the WL regime ($\kappa, \gamma \ll 1$), images of background sources are coherently but mildly distorted. In the WL regime ($\kappa, \gamma \ll 1$), images of background sources are coherently but mildly distorted. The weak lensing shear signal is far smaller than the intrinsic ellipticity scatter of background galaxies, making it undetectable for any individual background source. Statistical averaging over large ensembles of background sources is therefore required to measure the mean tangential shear profile, which traces the projected mass distribution at large radii. At group scales, the signal-to-noise per system is low and stacking over many systems is typically needed [Leauthaud et al., 2010].

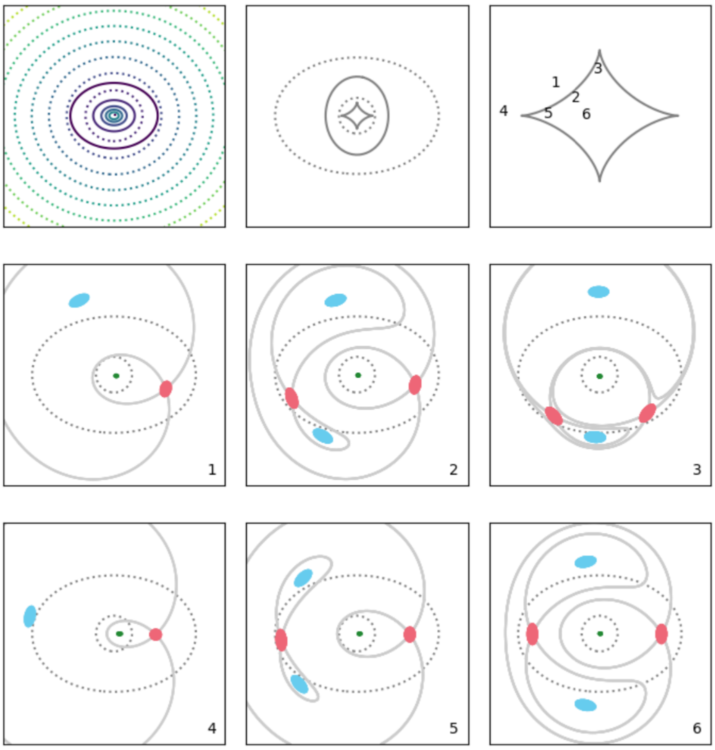

Figure 3.2: Lens and image properties for a PIEMD. The upper left panel shows contours of the surface density $\kappa(\theta)$ (solid curves) and the lensing potential $\psi(\theta)$ (dotted curves). The upper middle panel shows the critical curves (dotted) and caustic curves (solid). The upper right panel details the diamond caustic with numbered source positions corresponding to the panels below, which show critical curves (dotted), saddle-point contours (solid), and images (minima in light blue, saddle points in orange-red, maxima in green). (Credits: Saha et al. 2024)

In the SL regime, κ reaches or exceeds unity over some region of the lens plane, and the lens equation becomes multi-valued: multiple images of the same background source are produced. This gives rise to discrete, easily identifiable observational features - multiple image systems, arcs, and Einstein rings - that can be modeled on a per-system basis without any stacking. SL directly constrains the inner projected mass distribution, within and near the Einstein radius θ_E, and is rare at group scales but highly constraining when present (Limousin et al. [2009]). It is the primary lensing regime exploited in this work.

3.2.2 Multiple Images and Arcs

When a source lies inside a caustic, the lens equation admits multiple solutions, each corresponding to a distinct image of the same source. The number, parity, and positions of these images are determined by the topology of the caustic network and the location of the source relative to it (Saha et al. [2024]).

Tangential arcs are the most commonly observed SL feature. They form when a source lies close to the tangential caustic: the corresponding images are elongated perpendicular to the radius vector and appear near the tangential critical curve. Their curvature follows the shape of the critical curve and therefore traces the projected mass geometry of the lens.

Radial arcs are produced when a source lies close to the radial caustic; these images are elongated along the radius vector and appear inside the Einstein radius, between the BGG and the tangential arc. Radial arcs are rarer and intrinsically fainter than tangential arcs, but they carry complementary information about the inner slope of the mass profile, a key quantity for distinguishing NFW cusps from cores (see Section 2.1.4).

Einstein rings represent the limiting case of a perfectly aligned, circularly symmetric configuration, in which the source, lens, and observer are collinear and the image forms a complete ring at radius θ_E. Complete rings are rare; partial rings and strongly curved arcs are more common observationally. As established in Section 3.1.3, the ring radius directly yields the projected enclosed mass $M(< \theta_E)$ independently of any assumed mass model (Eq. 3.3).

At group scales, identifying and modeling these features is challenging. The BGG light contaminates the inner arc region, the lensing cross-section is lower than for massive clusters, and the angular scales involved demand high angular resolution. High-resolution space-based imaging - in particular from Hubble Space Telescope (HST) and James Webb Space Telescope (JWST) - is therefore essential for arc detection and morphological modeling.

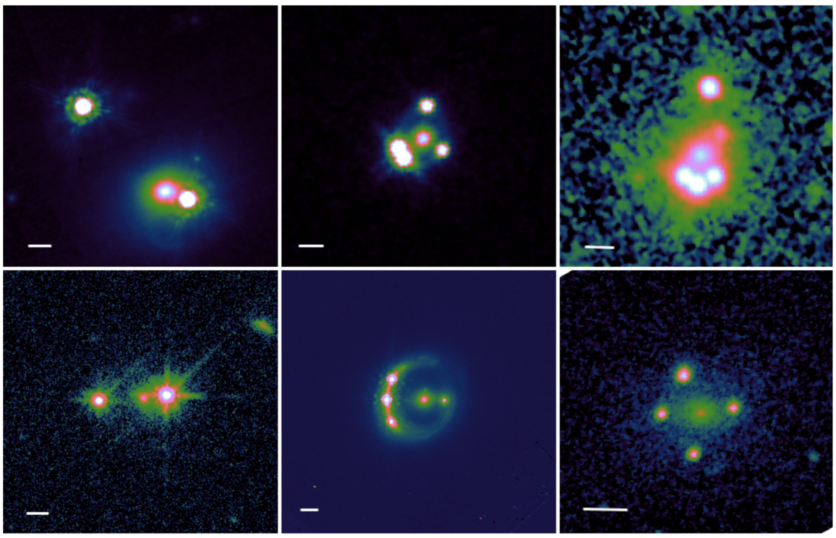

Figure 3.3: A collage of HST images of multiply-imaged lensed quasars, oriented so that image configurations correspond to the theoretical caustic configurations. Systems shown are (from top left) Q0957+561, PG1115+080, RXJ0911+0551, HE1104-1805, RXJ1131-1231, and Q2237+030. Tick marks indicate a $1''$ angular scale. (Credits: Saha et al. 2024)

3.2.3 Magnification

As defined in Eq. 3.5, the magnification μ is the ratio of the observed image solid angle to the intrinsic source solid angle, or equivalently the ratio of observed to intrinsic flux, since GL conserves surface brightness but alters the apparent solid angle (Bartelmann & Schneider [2001]).

In this work, magnification is not used as a direct observable. However, the high magnification of detected arcs provides two practical benefits. First, it increases the apparent angular size and SNR of background sources, enabling detailed morphological modeling of arc surface brightness distributions. Second, it effectively provides enhanced angular resolution in the source plane, allowing structure in the lensed source to be recovered through lens modeling. Both effects are exploited when modeling the arc morphology as a constraint on the projected mass distribution, as described in Section 3.3.

3.3 Mass Modeling

The observable signatures of strong gravitational lensing - image positions, arc morphologies, and flux ratios - are not direct mass maps but rather projections of the gravitational potential integrated along the line of sight. Extracting a physically meaningful mass model from these observables therefore requires a principled inference framework connecting the assumed mass distribution to the predicted lensed configuration. This section describes the forward modeling paradigm adopted throughout this thesis, the parametric mass profiles used to describe the different mass components of group-scale lenses, and the principal degeneracies that affect the interpretation of strong lensing mass models.

3.3.1 General Framework and Lenstronomy

The forward modeling paradigm proceeds as follows. A parametric mass model is assumed and computed using simulations. The predicted configuration is then compared to the observed one, and the model parameters are optimised so as to maximise a likelihood function. Two levels of comparison are commonly employed. In image-position fitting, only the centroids (and sometimes clearly identifiable key features of the source) of identified lensed images are used as constraints; this approach is computationally efficient but discards the spatial information encoded in the extended arc morphology. In surface-brightness fitting, the full pixel-level surface brightness distribution in the image plane is used as the likelihood, exploiting all available morphological information. Because our systems feature resolved arcs, we adopt the surface-brightness fitting approach throughout this work, which is the standard for systems with extended lensed emission (Saha et al. [2024]).

Model parameters are constrained within a Bayesian framework. The posterior distribution over the model parameters is sampled using Markov Chain

Monte Carlo (MCMC) or nested sampling algorithms, with priors encoding physical expectations - for example, the concentration-mass relation from ΛCDM simulations discussed in Section 2.1.3. This probabilistic treatment naturally propagates parameter uncertainties into derived quantities such as the Einstein radius, halo mass, and dark matter fraction (Birrer et al. [2021]).

All mass modeling presented in this thesis is performed using Lenstronomy (Birrer & Amara [2018], Birrer et al. [2021]), a Python-based open-source strong lensing analysis package. Lenstronomy supports a wide range of parametric mass and light profiles, Point Spread Function (PSF) convolution, multi-band fitting, and posterior sampling. It is widely used in the strong lensing community for galaxy-scale analyses but has not seen much usage for group-scale lensing. It serves as the primary computational tool for the analyses presented in Chapter 5 and subsequent chapters of this thesis.

3.3.2 Parametric Models

Parametric mass models assume a specific functional form for the projected surface mass density. Their main advantages are that they are physically motivated, involve a small number of free parameters, and produce predictions that can be directly compared to ΛCDM expectations. They are particularly well-suited to group-scale lenses, where the number of independent constraints from multiple-image systems is moderate - typically providing a few dozen to a few hundred surface-brightness constraints across the arc, rather than the thousands available for rich clusters (Meneghetti et al. [2017]). The following profiles are used as the building blocks of the mass models in this work.

Singular Isothermal Ellipsoid

The Singular Isothermal Ellipsoid (SIE) profile describes a mass distribution whose projected surface mass density scales as $\Sigma \propto 1/\xi$, where ξ is the elliptical radius. This corresponds to a three-dimensional singular isothermal sphere with an elliptical projected geometry. The SIE is parametrised by the Einstein radius θ_E (or equivalently the velocity dispersion σ_{SIE}, related by $\theta_E = 4\pi(\sigma_{\text{SIE}}/c)^2 D_{LS}/D_S$, which follows directly from Eq. 3.3), the projected axis ratio q, and the position angle ϕ. The deflection angles of the SIE have closed-form analytical expressions, making it computationally efficient. Its critical curve is an ellipse and its caustic is a diamond-shaped astroid.

The SIE produces a flat projected velocity dispersion profile, which is physically motivated for the innermost regions of massive elliptical galaxies where the combined contribution of stellar mass and the inner dark matter halo approximates an isothermal distribution (Koopmans et al. [2006]). A known limitation is the absence of a physical truncation radius, which causes the total projected mass to diverge logarithmically. This is not a concern within the strong lensing aperture, which lies well inside r_{200}, but means the SIE cannot be extrapolated to large radii. In this work, the SIE is used to model the BGG stellar and inner dark matter component.

NFW Profile

The NFW profile (Navarro et al. [1996]), introduced in Section 2.1.3 (Eq. 2.1), is physically motivated by ΛCDM N-body simulations and is used in this work to model the extended group-scale dark matter halo. In projection, the surface mass density $\Sigma(R)$ and the mean surface mass density $\bar{\Sigma}(< R)$ have closed-form analytical expressions (Oguri [2021]), which allow the convergence $\kappa_{\rm NFW}(R)$ and deflection angles to be computed efficiently. The NFW profile is parametrised by the characteristic density ρ_s and the scale radius r_s, or equivalently by the halo mass M_{200} and the concentration $c = r_{200}/r_s$. The concentration-mass relation $c(M, z)$ from ΛCDM simulations provides a physically motivated prior on these parameters (Navarro et al. [1996]), as discussed in Section 2.1.3.

A key limitation is that strong lensing alone cannot independently constrain both M_{200} and c without additional radial information, because both parameters contribute to the projected mass within θ_E. This concentration-mass degeneracy is discussed further in Section 3.3.3.

The NFW profile can also be modeled within a lensing pipeline using the Core-Softened Ellipsoid (CSE) basis set, a family of softened power-law profiles each characterised by a core radius s and a slope, which admit fully analytical lensing quantities. Oguri [2021] showed that the projected NFW convergence profile can be accurately decomposed as a finite sum of CSE components,

$$\kappa_{\rm NFW}(R) \approx \sum_i w_i\, \kappa_{\rm CSE}(R;\, s_i), \tag{3.6}$$

where each component is characterised by a core radius s_i and a weight w_i. Given the NFW parameters (ρ_s, r_s), the weights and core radii of the CSE expansion are determined by fitting the analytical surface mass density $\Sigma_{\rm NFW}(R)$ from Wright & Brainerd [2000]. In practice, a set of logarithmically spaced core radii $\{s_i\}$ spanning the relevant projected scales is chosen, and the corresponding weights $\{w_i\}$ are obtained by non-negative least-squares optimisation, ensuring that $\kappa_{\rm NFW}(R)$ is reproduced to high accuracy over the radial range of interest. The amplitude of each CSE component is related to the NFW characteristic surface mass density $\Sigma_s = \rho_s\, r_s$ through the normalisation of $\Sigma_{\rm NFW}$. This CSE representation is convenient because it inherits all the analytical lensing properties of the CSE basis - deflection angles, convergence, and shear - while encoding the physically motivated NFW mass distribution.

Combined Elliptical Galaxies and Halo Model

The core modeling strategy of this work is a multiple-component SIE + NFW decomposition. The SIEs represent the cores of the lensing galaxies, capturing the combined contribution of stellar mass and the inner dark matter distribution, while the NFW represents the extended group halo. This decomposition connects directly to the physical picture of galaxy group mass structure discussed in Section 2.3.3 and to the dark matter fraction analysis of Section 3.5.

External Shear

In practice, the lensing mass distribution is perturbed by tidal fields from large-scale structure along the line of sight and from neighbouring mass concentrations not explicitly included in the model. These perturbations are accounted for by adding a uniform external shear field, parametrised by the shear amplitude γ_{ext} and its position angle ϕ_{ext}. The external shear is always included as a free component in our models; its amplitude encodes the degree of environmental perturbation experienced by the group.

Other Profiles

For completeness, we briefly mention two additional families of profiles that appear in the strong lensing literature but are not used in this work. The PIEMD profile is a softened isothermal ellipsoid with a finite core radius and a truncation radius; it is widely employed in the Lenstool pipeline for cluster-scale analyses (Jullo et al. [2007]). Point mass, Hernquist, and de Vaucouleurs profiles are occasionally used to model the compact stellar component of the galaxies separately from the dark matter halo, in the context of mass decomposition analyses (Hernquist [1990]).

3.3.3 Degeneracies

Strong lensing mass models are subject to a number of well-known degeneracies that limit what can be inferred from the observables alone. We briefly describe the most relevant ones for the analysis presented in this thesis.

Mass-Sheet Degeneracy

The mass-sheet degeneracy (Mass-Sheet Degeneracy (MSD)) is the fundamental degeneracy of gravitational lensing (Gorenstein et al. [1988]). Any convergence field $\kappa(\theta)$ can be transformed as

$$\kappa'(\theta) = \lambda\, \kappa(\theta) + (1 - \lambda), \tag{3.7}$$

with a simultaneous rescaling of the source position ($\beta' = \lambda\beta$), leaving all image positions, shapes, and flux ratios unchanged. Only observables that depend on the absolute magnification - such as time delays between lensed images or standard-candle source fluxes - break this degeneracy (Saha et al. [2024]). Parametric models partially break the MSD by imposing a specific functional form for $\kappa(\theta)$, but the residual external convergence κ_{ext} from line-of-sight mass structure remains a systematic uncertainty. In the context of group-scale lensing, the MSD is understood as a known systematic whose amplitude is typically constrained using external information or through priors on the line-of-sight mass distribution (Birrer et al. [2021]).

The time delay between image pairs in a multiply-imaged system depends on the so-called *time-delay distance*

$$D_{\Delta t} \equiv (1 + z_L) \frac{D_L D_S}{D_{LS}}, \tag{3.8}$$

which combines the three angular diameter distances of the configuration. $D_{\Delta t}$ sets the overall scale of the Fermat potential difference and therefore enters directly into any Hubble constant inference from time-delay cosmography (Saha et al. [2024]). Although time delays are not measured in this work, $D_{\Delta t}$ characterises the lensing geometry and is quoted when describing the ACO 3827 configuration.

Concentration-Mass Degeneracy

For NFW profiles, strong lensing primarily constrains the projected mass enclosed within the Einstein radius θ_E, but the individual parameters M_{200} and c are partially degenerate because different combinations of halo mass and concentration can produce the same Einstein radius. Breaking this degeneracy requires either additional radial constraints - from weak lensing at large radii, X-ray observations, or member galaxy velocity dispersions - or a strong prior from the ΛCDM concentration-mass relation (Navarro et al. [1996]). In this work, the concentration-mass prior is used to help break the degeneracy, as described in Chapter 5.

BGG-Halo Decomposition Degeneracy

Decomposing the total projected mass into a BGG component and a group halo component is inherently degenerate without an independent constraint on the stellar mass. Both components contribute to the convergence within the Einstein radius, and strong lensing alone cannot disentangle them. An independent stellar mass estimate for the lensing galaxies obtained from photometric Spectral Energy Distribution (SED) fitting or from an assumed stellar mass-to-light ratio is needed.

3.4 Radial Mass Profile and Mass Decomposition

Having established the parametric mass models used in this work (Section 3.3), we now turn to what can be inferred about the underlying radial mass distribution once a model has been optimised. This section discusses how the total projected mass is computed from the lens model, how it can be deprojected into a three-dimensional estimate, and how the total mass is decomposed into its baryonic and dark matter components. These steps are central to the scientific objectives of this thesis, since the primary goal is to characterise the dark matter content of group-scale haloes at intermediate masses.

3.4.1 Projected and Enclosed Mass

The most robustly constrained quantity from SL modeling is the total projected mass enclosed within the Einstein radius θ_E. As shown in Equation 3.3, the Einstein radius is defined by the condition that the mean convergence within that radius equals unity, which leads directly to the projected mass estimate

$$M(<\theta_E) = \pi\theta_E^2\,\Sigma_{\rm cr}\,D_L^2, \tag{3.9}$$

where $\Sigma_{\rm cr}$ is the critical surface mass density and D_L is the angular diameter distance to the lens. This quantity is essentially model-independent: as long as θ_E is accurately measured from the image geometry, the projected mass within it is robustly constrained regardless of the assumed radial profile shape (Saha et al. [2024]; Koopmans et al. [2006]).

Beyond the Einstein radius, the radial distribution of mass is encoded in the projected surface mass density profile $\Sigma(R)$ and in the mean surface density within projected radius R,

$$\bar{\Sigma}(<R) = \frac{M_{\rm 2D}(<R)}{\pi R^2}. \tag{3.10}$$

These quantities depend on the assumed parametric model (Section 3.3.2). For the NFW profile, closed-form analytical expressions for both $\Sigma(R)$ and $\bar{\Sigma}(<R)$ are available (Wright & Brainerd [2000]), allowing the convergence profile and deflection angles to be computed efficiently at any projected radius. For the SIE), the projected mass profile is likewise analytical, and the total projected mass within the Einstein radius is directly related to the velocity dispersion $\sigma_{\rm SIE}$.

Converting from a projected mass profile to a three-dimensional enclosed mass $M_{\rm 3D}(<r)$ requires deprojection, which is inherently model-dependent. As discussed in Section 3.3.2, the NFW profile has well-defined three-dimensional expressions at all radii, and the conversion between $M_{\rm 2D}$ and $M_{\rm 3D}$ is consistent within the same analytical framework (Navarro et al. [1996]). The SIE, by contrast, does not correspond to a unique three-dimensional density distribution: it is a projected model, and multiple three-dimensional profiles are compatible with the same observed convergence map. This introduces an irreducible uncertainty when estimating the three-dimensional mass contribution of the BGG component, which is propagated explicitly in the analysis presented in Chapter 7.

As introduced in Section 2.3.1, all masses in this work are expressed using the M_{200} convention, corresponding to the total mass enclosed within r_{200}, the radius at which the mean interior density equals 200 times the critical density of the Universe at the lens redshift. At group scales, r_{200} typically lies well beyond the strong lensing Einstein radius, meaning that M_{200} cannot be measured directly from SL alone and must be extrapolated from the best-fitting radial profile. The uncertainty associated with this extrapolation is discussed in Chapter 6.

3.4.2 Stellar versus Total Mass Decomposition

Strong lensing measures the total projected mass within the Einstein radius, encompassing all mass components along the line of sight: the extended dark matter halo, the stellar mass of the lensing galaxies, the contributions of satellite galaxies within the group, and the diffuse gas of the IGrM. Isolating the dark matter contribution therefore requires either complementary observational probes or physically motivated prior assumptions about the non-dark-matter components (Meneghetti et al. [2017]).

The decomposition strategy adopted in this work is as follows. The lensing galaxies are modeled as separate mass components using SIE profiles (Section 3.3.2), whose velocity dispersion normalisation is constrained either by the lensing data or by a prior derived from the photometric stellar mass. The group-scale dark matter halo is modeled as an NFW profile (Section 3.3.2), and the two components are optimised simultaneously against the observed arc positions.

3.5 Dark Matter Fraction

The dark matter fraction $f_{\rm DM}$ is a fundamental quantity that encodes the relative contribution of dark matter to the total mass budget of a system within a given aperture. At group scales, it connects directly to the SHMR (Section 2.3.4), the baryonic content of the IGrM (Section 2.3.2), and the dark matter halo properties discussed in Section 2.3.3. This section defines $f_{\rm DM}$ and discusses its aperture dependence, its radial behaviour across different mass scales, and its connection to scaling relations relevant to cosmological applications.

3.5.1 Definition and Aperture Dependence

The dark matter fraction within a projected aperture R is defined as the ratio of the dark matter mass to the total projected mass enclosed within that aperture:

$$f_{\rm DM}(< R) = \frac{M_{\rm DM}(< R)}{M_{\rm tot}(< R)}, \tag{3.11}$$

where $M_{\rm tot}(< R)$ is obtained from gravitational lensing and $M_{\rm DM}(< R)$ is derived by subtracting the projected baryonic mass from this total. In this work, the baryonic component is modeled through the stellar light distribution of the BGG and any additional member galaxies, represented by SED-fitted SIE or Sersic profiles (Section 3.3).

Aperture dependence is a fundamental feature of $f_{\rm DM}$: the value of the dark matter fraction changes substantially with the radius at which it is evaluated, and any quoted value of $f_{\rm DM}$ is therefore meaningless without a specification of the aperture. At group scales, the BGG stellar mass dominates the mass budget at small projected radii ($R \lesssim R_e$, where R_e is the half-light radius of the BGG, typically a few kiloparsecs), while the extended NFW halo becomes the dominant contribution at larger radii. As a result, $f_{\rm DM}$ rises steeply with radius across the range probed by gravitational lensing.

Three aperture choices are commonly adopted in the literature and each carries a distinct physical meaning. The Einstein radius θ_E is the most directly constrained aperture from strong lensing, as it corresponds precisely to the region within which the critical surface mass density condition is satisfied. The effective radius R_e of the BGG allows direct comparison with galaxy-scale strong lensing studies such as the SDSS Lens ACS Survey (SHMR; Koopmans et al. [2006]). Finally, the virial radius r_{200} provides the aperture most directly relevant to cosmological baryon fraction measurements, but it requires significant extrapolation beyond the radii constrained by lensing. In this work, results are primarily quoted within the Einstein radius and within R_e, where the lensing constraints are most direct.

3.5.2 Radial Trend and Comparison Across Mass Scales

At group scales, the radial profile of $f_{\rm DM}$ reflects the transition from a baryon-dominated centre to a dark-matter-dominated outskirt. Within R_e, dark matter fractions in the range $\sim$ 30-60% are expected, rising to $\sim$ 85-95% at r_{200} as the NFW halo contribution increasingly dominates over the stellar component (Kravtsov & Borgani [2012]). This behaviour is a direct consequence of the structural difference between the compact stellar distribution of the BGG and the much more extended dark matter halo in which it resides (Section 2.3.3).

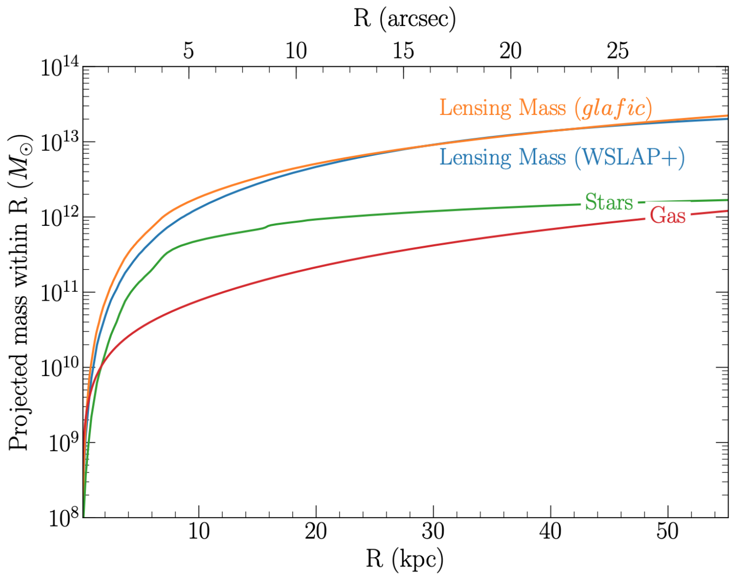

Figure 3.4: Illustration of the expected radial trend of $f_{\rm DM}$ at group scales (here the A3827 group), showing the transition from baryon-dominated centres to dark-matter-dominated outskirts. (Credits: Chen et al. [2020]

Comparing across mass scales provides crucial context for interpreting group-scale measurements. At galaxy scales, the peak of the SHMR at $M_{\text{halo}} \sim 10^{12}\,\text{M}_\odot$ implies a high stellar-to-halo mass ratio, which results in relatively low f_{DM} at small projected radii. Strong lensing studies of early-type galaxies have measured dark matter fractions within R_e of order 20-40%, consistent with the baryon-dominated interiors of L^* galaxies (Koopmans et al. [2006]). In contrast, group-scale systems lie above the SHMR peak where star formation efficiency is suppressed by AGN feedback (Section 2.3.4), meaning that the stellar mass grows more slowly than the halo mass. Groups are therefore more dark-matter-dominated than L^* galaxies at all projected radii, despite hosting a luminous BGG at their centre.

At cluster scales, f_{DM} is similarly high at all radii; however, the hot ICM constitutes an additional baryonic component that is largely absent in groups, reducing the dark matter fraction relative to a purely stellar baryonic baseline (Pratt et al. [2019]). Galaxy groups therefore occupy a transition regime in which the stellar mass of the BGG is the dominant baryonic component at small radii, the IGrM provides a subdominant but non-negligible contribution at intermediate radii, and the dark matter halo dominates at all scales beyond a few effective radii. This combination makes groups the most dark-matter-dominated environment per unit stellar mass across the full halo mass function (Behroozi et al. [2013]), as reflected in their peak mass-to-light ratios of $\sim$ 100-300 $\text{M}_\odot/\text{L}_\odot$ (Section 2.3.3).

Observational constraints on f_{DM} at group scales from strong lensing remain sparse. Early analyses using SL in group-scale systems have demonstrated the feasibility of decomposing the mass into stellar and dark matter components within the Einstein radius, but the sample sizes and photometric depth of available data have limited the precision of these measurements (Limousin et al. [2009]; Thanjavur et al. [2010]). More recent studies have begun to exploit deep imaging from the HST to identify multiply-imaged systems in serendipitously discovered group-scale lenses, progressively building a statistical picture of f_{DM} at intermediate mass scales. A key objective of this work is to extend and improve this observational picture through the multiwavelength analysis presented in the following chapters.

3.5.3 Connection to Scaling Relations

The dark matter fraction is not an isolated quantity; it is intimately connected to the scaling relations that link observable properties to halo mass. At fixed halo mass, a higher stellar-to-halo mass ratio implies a lower f_{DM} at any given projected aperture, so that scatter in the SHMR translates directly into scatter in f_{DM}. Conversely, a robust measurement of f_{DM} from lensing, combined with an independent stellar mass estimate from photometric or spectroscopic modeling, provides a direct constraint on the position of a given system relative to the mean SHMR. This makes lensing-based dark matter fractions a valuable tool for calibrating the SHMR at group scales, where other mass proxies are subject to larger systematic uncertainties (Section 2.3.4).

The gas fraction of the IGrM introduces an additional baryonic component whose contribution to $f_{\rm DM}$ is mass-dependent. As discussed in Section 2.3.2, the gas fraction scales approximately as $f_{\rm gas} \propto M^{0.3}$ (Sun et al. [2009]), meaning that the baryonic fraction has a systematic mass dependence. Neglecting the IGrM gas contribution when computing $f_{\rm DM}$ therefore leads to a systematic overestimate of the dark matter fraction that is more severe at lower halo masses. In this work, the IGrM contribution is not directly incorporated into the lensing mass decomposition, since the gas distribution is not independently constrained for all systems in the sample; this represents a source of systematic uncertainty that is discussed further in the analysis chapters.

At the virial radius, the dark matter fraction $f_{\rm DM}(< r_{200})$ is directly related to the complement of the total baryon fraction:

$$f_{\rm DM}(< r_{200}) = 1 - f_{\rm bar}(< r_{200}) = 1 - f_\star(< r_{200}) - f_{\rm gas}(< r_{200}), \qquad (3.12)$$

where $f_\star$ and $f_{\rm gas}$ are the stellar and gas mass fractions respectively. The baryon fraction in groups and clusters has long been recognised as a cosmological probe, since the ratio $f_{\rm bar} \approx \Omega_b/\Omega_m$ provides a direct constraint on the matter density parameter (Fukugita et al. [1998]). Lensing-based measurements of $f_{\rm DM}$ at group scales therefore offer an independent calibration of this cosmological quantity, complementing X-ray baryon fraction measurements that are subject to the hydrostatic mass bias discussed in Section 2.3.4.

3.6 Group-Scale Strong Lensing: State of the Art

This section reviews the current observational landscape of SL studies at group scales. After motivating why group-scale lenses are both rare and scientifically valuable, we survey the known population of systems and the key results they have established. We then outline the prospects offered by ongoing and future surveys, before closing with a discussion of multi-wavelength synergies that form the methodological backbone of this thesis.

3.6.1 Why Group-Scale Lenses Are Rare and Scientifically Valuable

The efficiency with which a mass concentration produces strong lensing is quantified by its lensing cross-section, which scales steeply with mass as $\sigma_{\rm lens} \propto \theta_{\rm E}^2 \propto M^{4/3}$, where $\theta_{\rm E}$ is the Einstein radius (Bartelmann & Schneider [2001]). As a result, individual galaxy groups are far less efficient lenses than massive clusters of comparable volume. The probability that a given group produces a detectable strong lensing configuration is correspondingly low, which explains why confirmed group-scale lens systems remain comparatively rare despite decades of survey work.

Nevertheless, groups are approximately two orders of magnitude more numerous than clusters at fixed redshift, as dictated by the exponential high-mass cutoff of the HMF (Section 2.1.5). The integrated number of group-scale lenses in the Universe is therefore large in an absolute sense; the principal challenge is their identification in wide-area, high-resolution imaging surveys where their more modest arc radii ($\theta_E \sim$ 5-15 arcsec) and lower surface brightness arcs can be confused with other morphological features (Limousin et al. [2009]).

The scientific value of group-scale lenses is disproportionate to their number. Groups occupy the transitional mass regime $M_{200} \sim 10^{13}$-$10^{14}\,M_\odot$, where the BGG stellar mass and the extended dark matter halo contribute comparably to the projected mass within the Einstein radius. This property makes group-scale lenses uniquely sensitive to the dark matter-baryon decomposition of the inner mass profile, a decomposition that is poorly accessible at either galaxy or cluster scales (Thanjavur et al. [2010]). Furthermore, as discussed in Section 2.3.3, the inner slope of the dark matter profile at group scales - whether cusp-like as predicted by NFW or shallower due to baryonic feedback - remains an open observational question. Strong lensing, as the most direct probe of the projected mass within θ_E, is the most powerful tool currently available to address it.

3.6.2 Discovered Systems and Key Results

The known population of well-characterised group-scale strong lenses currently numbers of order a few tens of systems, compared to hundreds of cluster-scale lenses and thousands of galaxy-scale lenses. This relative scarcity reflects the combined effect of the low lensing cross-section per system and the historical dominance of survey strategies optimised for either galaxy-scale or cluster-scale lenses. Several dedicated programmes have nonetheless established the observational basis for group-scale SL science.

The Strong Lensing Legacy Survey (SL2S) (Limousin et al. [2009]) was the first systematic search for group-scale lenses, conducted in imaging data from the Canada-France-Hawaii Telescope Legacy Survey. SL2S identified a sample of group-scale lens candidates by targeting extended arc-like features around luminous red galaxies and compact group cores. Follow-up analysis of the SL2S sample confirmed that the projected masses enclosed within the Einstein radius are broadly consistent with NFW mass profiles, and provided the first statistical constraints on the lensing cross-section at group scales (Limousin et al. [2009]). A joint strong lensing and dynamics analysis of a subset of SL2S systems further established that the dark matter fraction within the Einstein radius is substantial and consistent with expectations from ΛCDM simulations (Thanjavur et al. [2010]).

The Cambridge And Sloan Survey Of Wide ARcs in the skY (CASSOWARY) catalogue (Stark et al. [2013]) extended the optically selected group-lens sample by exploiting visual inspection of SDSS imaging. CASSOWARY provided the first large homogeneous sample of group-scale lenses selected purely on optical morphology, enabling statistical studies of the group lens population independently of X-ray selection.

Current observational constraints from these programmes establish Einstein radii in the range 5-15 arcsec for group-scale lenses, corresponding to projected masses of 10^{13}-$10^{14}\,M_\odot$ within θ_E. Concentration parameters are broadly consistent with ΛCDM predictions from the concentration-mass relation (Navarro et al. [1996]), though the inner slope and the cusp-core distinction remain poorly constrained for most systems due to the limited number of multiple image families available in group-scale configurations (Limousin et al. [2009]; Monna et al. [2014]).

3.6.3 Ongoing and Future Surveys

The coming decade will transform the statistical basis of group-scale SL science through a new generation of wide-field imaging surveys with substantially improved depth and angular resolution.

The Euclid space telescope, launched in 2023, is conducting a wide-field optical and near-infrared survey covering approximately 15,000 deg^2 of the extragalactic sky. The Visible Imager (VIS) instrument provides optical imaging at 0.1 arcsec resolution, sufficient to resolve arcs and multiple image configurations at group scales across the full survey area. While existing forecasts for lens discoveries in upcoming surveys such as *Euclid* and the Vera C. Rubin Observatory Legacy Survey of Space and Time (LSST) focus on galaxy-scale deflectors (Collett [2015]), the sheer survey volume and depth of these missions are expected to yield a corresponding increase in the discovery of group-scale systems as well, substantially expanding the known population beyond the few tens of systems currently comprising the SL2S and CASSOWARY samples (Limousin et al. [2009]; Stark et al. [2013]). The Near Infrared Spectrometer and Photometer (NISP) instrument additionally provides near-infrared photometry and slitless spectroscopy, enabling photometric redshift estimates for both lens and source.

The LSST at the Vera C. Rubin Observatory (LSST Science Collaboration et al. [2009]) will complement Euclid with deep, multi-band optical imaging over a comparable sky area, reaching significantly greater depth over its ten-year baseline.

The JWST is not a survey instrument but provides the highest-resolution follow-up imaging currently available, with angular resolution of approximately 0.06 arcsec in the Near Infrared Camera (NIRCam) F200W band. For known group-scale lenses, JWST observations reveal the detailed morphology of lensed arcs, faint multiple images that are undetectable from the ground, and the resolved structure of the BGG at the centre of the group, all of which are critical inputs for high-precision mass modeling.

In the X-ray domain, the extended ROentgen Survey with an Imaging Telescope Array (eROSITA) telescope aboard the SRG spacecraft is conducting an all-sky X-ray survey with sensitivity and angular resolution substantially exceeding the previous ROSAT all-sky survey. eROSITA is expected to detect of order 10^5 galaxy groups and clusters (Pillepich et al. [2012]), producing the largest X-ray selected group catalogue to date. The combination of eROSITA group catalogues with strong lensing detections from Euclid and Rubin will enable systematic joint X-ray and lensing analyses at group scales for the first time, directly extending the multi-wavelength approach adopted in this thesis.

Spectroscopic follow-up remains essential for confirming group membership, measuring spectroscopic redshifts of lensed sources, and obtaining stellar velocity dispersions of the BGG as an independent kinematic mass constraint. Integral-field spectrographs such as Multi Unit Spectroscopic Explorer (MUSE) at the Very Large Telescope (VLT) are particularly powerful in this context, providing simultaneous spectra over the full group core in a single pointing and enabling the identification of multiply imaged source components through their common redshift.

Chapter 4

Target of Interest: ACO 3827

This chapter introduces ACO 3827, the galaxy group that is the subject of this thesis. After reviewing its discovery and prior observations, we describe the group membership, lensing geometry, multiband appearance, and the diffuse intra-group light that makes it a particularly interesting system for the analysis developed in this work.

4.1 Discovery and Prior Observations

ACO 3827 (also known as Abell 3827) is a galaxy group at redshift $z = 0.099$, catalogued in the Abell survey of clusters of galaxies (Abell et al. [1989]). The system was initially classified as a galaxy cluster owing to its dense core appearance in optical imaging, but its total mass, X-ray luminosity, and galaxy velocity dispersion place it in the group-to-poor-cluster transition regime, with a total halo mass $M_{200} \sim 10^{13}$-$10^{14}\,\mathrm{M}_{\odot}$.

ACO 3827 first attracted significant astrophysical interest through its strong gravitational lensing, with an Einstein ring-like arc system first characterised in detail by Carrasco et al. [2010]. The system subsequently became the subject of a notable series of observations motivated by claims of an offset between the dark matter halo of one of its central galaxies and its stellar component, interpreted as a possible signature of self-interacting dark matter (Williams & Saha [2011]; Mohammed et al. [2014]; Massey et al. [2015]). Later re-analysis with deeper HST data showed that this offset is consistent with zero within the measurement uncertainties when a more complete modeling of the stellar and Intra-Group Light (IGL) components is performed (Massey et al. [2018]). ACO 3827 therefore represents a system where careful photometric and mass modeling - precisely the approach taken in this thesis - is critical for reaching robust physical conclusions.

4.2 Group Membership and Redshifts

The lensing core of ACO 3827 (as presented in Figure 4.1) is dominated by four massive early-type galaxies in close projected proximity, separated by only a few arcseconds. These four galaxies, labelled G1 through G4 in this work, form the effective lens for the background source. Their positions, measured from the simultaneous Sérsic fit described in section 5.3, are listed in Table 4.1. Galaxy G2 is adopted as the coordinate reference and corresponds to the galaxy nearest to the photometric center of the group.

Galaxy	$\Delta\alpha$ [$''$]	$\Delta\delta$ [$''$]
G1	-5.143	-2.002
G2	0.000	0.000
G3	$+4.166$	-3.095
G4	$+4.610$	$+1.927$

Table 4.1: Positions of the four lensing group galaxies in ACO 3827, expressed as arcsecond offsets from the center of galaxy G2. All four galaxies are at $z \approx 0.099$.

The lensed background source is at redshift $z_s = 1.24$. For a flat ΛCDM cosmology with $H_0 = 70\,\mathrm{km\,s^{-1}\,Mpc^{-1}}$ and $\Omega_m = 0.3$, this yields $D_{LS}/D_S = 0.89$ and an effective time-delay distance $D_{\Delta t} = 699.9\,\mathrm{Mpc}$. The resulting Einstein radius for this configuration is $\theta_E \approx 10''$.

4.3 Lensing Geometry

The lensing configuration in ACO 3827 is remarkably complete. The background source at $z_s = 1.24$ is quadruply imaged, with four distinct arc images (labeled arcs 1-4) distributed around the group core at projected radii of approximately 5-15$''$. This angular scale corresponds to the Einstein radius regime of a group-scale lens (section 2.3), confirming that the total projected mass within $\sim 10''$ is of order 10^{12}-10^{13} $M_\odot$. Clusters on the other hand have larger Einstein radius ranging from 15" to 50" (Fox et al. [2022]).

The arcs are connected by lower-surface-brightness emission that traces the extended source morphology, including what appears to be a partial Einstein ring-like structure in the reddest image. Bright emission knots are visible on the arcs across multiple images, tracing compact star-forming regions within the background source galaxy.

The proximity of the four lensing galaxies to each other and to the arc images makes this system more complex than a single-galaxy strong lens. The total projected mass within the Einstein ring is contributed jointly by all four group members, rather than being dominated by a single BGG as in simpler lensing configurations. This motivates the multi-component SIE parametrisation described in chapter 5.

4.4 Multiband Imaging

Figure 4.1 shows a three-colour composite image of the ACO 3827 core constructed from the F336W (blue), F606W (green), and F814W (red) HST bands. The four group galaxies appear in warm red, reflecting their evolved stellar populations with little star formation. The lensed arcs are strikingly blue, consistent with the rest-frame ultraviolet emission of a star-forming galaxy at $z_s = 1.24$, which is shifted into the F336W and F606W passbands at this redshift. The characteristic curved morphology of the arc emission, wrapping around the group core in a partial Einstein ring geometry, makes ACO 3827 an excellent system for visual identification and astrometric measurement of the arc features. The superposition of arc emission on the extended envelopes of the group galaxies makes it clear that careful lens light subtraction is essential before any quantitative arc analysis can be performed.

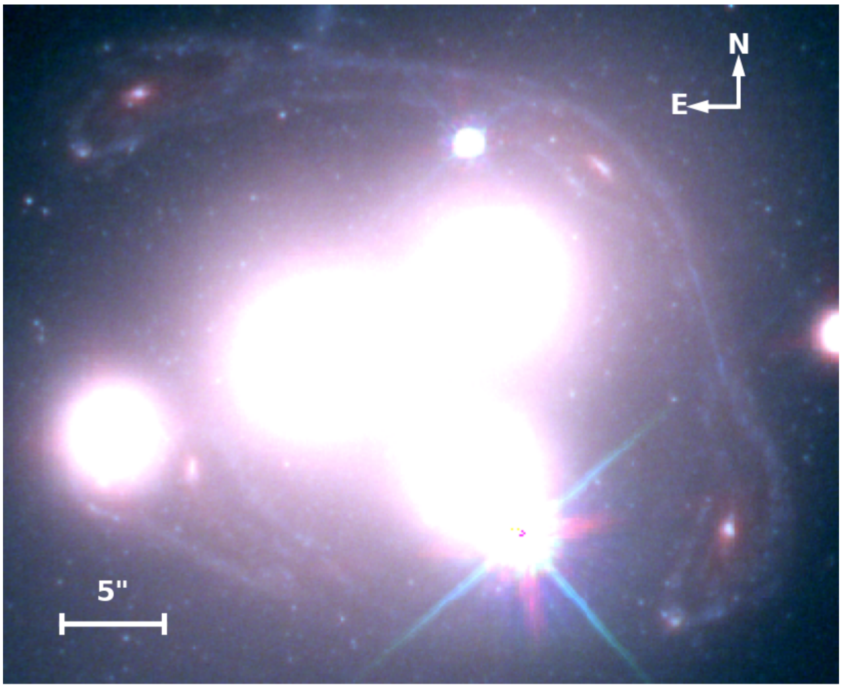

Figure 4.1: Three-colour HST composite image of ACO 3827 (F336W = blue, F606W = green, F814W = red). The four red early-type group galaxies forming the lens are surrounded by four blue arc images of the $z_s = 1.24$ background source. Extended arc emission connecting the four main images and the diffuse intra-group light are also visible.

The F814W band used for all quantitative modeling captures the rest-frame optical continuum of the group galaxies (dominated by the old stellar population) and simultaneously the rest-frame near-ultraviolet emission of the background source, making it the optimal single-band choice for joint lens and arc modeling.

4.5 Intra-group light

A faint diffuse emission is visible between the four group galaxies in the deep HST imaging, extending well beyond the effective radii of any individual member. This IGL is the mainly comes from stars stripped from their parent galaxies over the assembly history of the group, and is the group-scale equivalent of intra-cluster light observed in massive clusters (Mihos et al. [2005]; Montes [2022]). At the redshift of ACO 3827 and with the HST resolution and depth available, the IGL manifests as a low-level, approximately uniform surface brightness excess that fills the space between the four lens galaxies.

The presence of IGL in the lens plane introduces a systematic in the surface brightness modeling: if it is not accounted for, the residual image after galaxy subtraction will contain a spurious positive background that could be misinterpreted as arc emission or could bias the normalisation of the arc surface brightness model. Conversely, over-modeling the IGL risks subtracting real arc flux. Subsection 7.1 describes the strategy adopted to parametrise and propagate the uncertainty in the IGL level, and its impact on the lens model is assessed through a direct comparison between models fitted with and without an explicit IGL component.

Chapter 5

Methodology

This chapter describes the observational data and the analysis framework developed to model the strong gravitational lens system ACO 3827 (see chapter 4). The workflow proceeds in three sequential stages.

First, the surface brightness distribution of the four group galaxies acting as the lens is modeled and subtracted from the science image, isolating the lensed source arc emission and characterising the IGL.

Second, a conjugate-point analysis uses the positions of identifiable features in the arcs as astrometric constraints to optimise the lens mass model independently of any assumption about the source surface brightness.

Third, the conjugate-point mass solution is used as the starting point for a full surface-brightness reconstruction in which the lens light, lens mass, and source light are fitted simultaneously.

It is important to note that while one could jump directly to the third step; without any good starting point for the full surface-brightness reconstruction, the simulation process cannot be "brute-forced" into a good model as it gets stuck in local minima during the optimisation process. It is therefore necessary to follow this 3-step procedure in order to get a satisfying model.

The tools, parametrisations, and calibration choices made at each stage are described in detail in the following sections.

5.1 Data

The primary dataset consists of HST observations of ACO 3827 obtained with the Advanced Camera for Surveys (ACS/WFC) and the Wide Field Camera 3 (WFC3). The available imaging spans four filters: F336W, F606W, F814W, and F160W, covering rest-frame ultraviolet through near-infrared wavelengths ($\sim$336-1600 nm; see Figure 5.1).

All quantitative modeling is performed on the F814W image (obtained with the ACS/WFC), as this band looks appears to offer the highest signal-to-noise for the lensed source. The full mosaic has a native pixel scale of $\Delta\theta = 0.050''$, and a 500×500 pixel ($25'' \times 25''$) sub-image centered on the group core is extracted

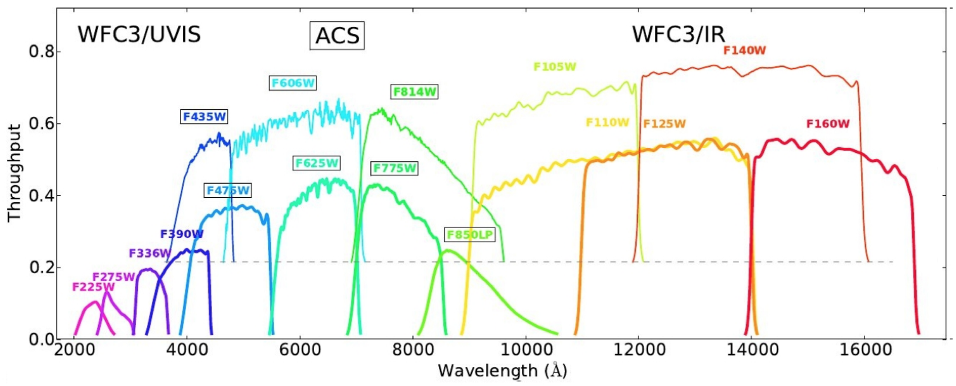

Figure 5.1: Transmission curves of the HST/ACS and HST/WFC3 filters used in this work (Credits: Monna et al. 2014).

for all subsequent analysis. The corresponding weight map and exposure-time map are extracted from the same Flexible Image Transport System (FITS) file and used to construct the per-pixel noise model described below.

5.1.1 Noise model

A realistic per-pixel noise map $\sigma(x, y)$ is essential for accurate surface-brightness fitting and for a meaningful χ^2 evaluation of the models. The noise map is constructed as

$$\sigma(x, y) = \sqrt{\tilde{I}(x, y) + \sigma_{\rm bg}^2(x, y)}, \tag{5.1}$$

where $\tilde{I}(x, y)$ is a locally smoothed version of the science image, expressed in electrons, obtained by convolving with a Gaussian of $\sigma_{\rm smooth} = 2$ pixels (to suppress pixel-level noise while preserving the signal gradient), and $\sigma_{\rm bg}^2 = 1/w(x, y)$ is the background noise variance estimated from the inverse of the DrizzlePac weight map $w(x, y)$. Since the drizzled science image is in units of counts $\rm s^{-1}$, $\tilde{I}(x, y)$ is multiplied by the total exposure time $t_{\rm exp}$ prior to use in Eq. (5.1) to ensure the Poisson term is in consistent units of electrons. This formulation captures both the Poisson contribution from source photons and the spatially variable background due to drizzling artifacts and variations in effective exposure time across the mosaic.

Read-out noise ($\sigma_{\rm RON} \approx 4\,{\rm e}^-$ per read for ACS/WFC) is not included explicitly in Eq. (5.1). For the bright lens galaxies, the Poisson term dominates and read-out noise is negligible. In the faint arc regions, the effective read-out noise per pixel is reduced by a factor $\sqrt{N_{\rm exp}}$ across the $N_{\rm exp} = 16$ combined exposures, bringing it to $\sigma_{\rm RON}/\sqrt{N_{\rm exp}} = 4/\sqrt{16} = 1\,{\rm e}^-$, which is subdominant relative to the background term $\sigma_{\rm bg}$ in the arc regions. Read-out noise is therefore considered negligible for the purpose of this analysis. Pixels with non-finite weight values are assigned the maximum finite noise value in the map.

5.2 Point Spread Function

The Point Spread Function (PSF) describes the response of an imaging system to a point source: any observed image is the convolution of the true sky brightness distribution with the PSF, which encodes the combined effects of diffraction, optical aberrations, and detector sampling. For HST, the PSF is spatially structured and relatively stable, but varies with field position and telescope focus state. Accurate modeling of the PSF is therefore critical for separating closely spaced components and for recovering the intrinsic morphology of the lensed arcs. The PSF for the F814W band is retrieved using TinyTim (Space Telescope Science Institute [2004]), a ray-tracing model of the HST optical system that accounts for telescope focus, field position, and detector geometry. 16 TinyTim models are generated at focus offsets ranging from $f = -10$ and $f = +5$ (in units of the secondary mirror position) to bracket the in-flight focus state of the telescope at the time of the ACO 3827 observations.

The PSF kernel used in all modeling is the TinyTim model at $f = -2$, cropped to a 99×99 pixel stamp centered on the position of the lensing group at pixel coordinates $(3700, 4100)$ in the full mosaic. A centering correction of $(+2, +4)$ pixels relative to the raw TinyTim model origin is applied to align the PSF peak with the center of its central pixel. This last step is necessary to make sure the PSF is aligned with the central pixel of the observation frame.

5.3 Lens Light Modeling

Computing the mass parameters directly without good initial estimates proved to be rather complicated. In order to better constrain the lens mass parameters, the surface brightness of the four group galaxies can be used as a stating point. To find these surface brightness parameters, they must be subtracted from the science image to expose the faint lensed arcs that lie in their immediate vicinity. This is done by fitting parametric light profiles to each galaxy using Lenstronomy (Birrer & Amara [2018]; Birrer et al. [2021]) in its galfitting mode. In this first stage, the lensing deflections are switched off and the lens light model is compared directly to the observed image.

5.3.1 Profile parametrisation

Each of the four group galaxies is modeled as an elliptical Sérsic profile (Sérsic [1963]), whose surface brightness is given by

$$I(R) = I_{\mathrm{e}} \exp\left\{ -b_n \left[\left(\frac{R}{R_{\mathrm{e}}} \right)^{1/n} - 1 \right] \right\}, \tag{5.2}$$

where R_{e} is the effective (half-light) radius, n is the Sérsic index, I_{e} is the surface brightness at R_{e}, and b_n is a normalisation constant defined such that half the total flux lies within R_{e}. The ellipticity is described by the two complex ellipticity components (e_1, e_2), which encode the axis ratio and position angle following this relations: $e_1 = e\cos(2\phi)$ and $e_2 = e\sin(2\phi)$. From these components, the standard ellipticity is calculated as $e = \sqrt{e_1^2 + e_2^2}$, and the position angle is determined by $\phi = \frac{1}{2}\,\mathrm{atan2}(e_2, e_1)$. In Lenstronomy, the amplitude of each profile is treated as a linear parameter and solved analytically during each likelihood evaluation, making the non-linear parameter space six-dimensional per galaxy: $(R_\mathrm{e}, n, e_1, e_2, x_c, y_c)$ with profile center (x_c, y_c).

A uniform surface brightness component (a constant background) is added to the model to capture any residual intra-group light that is not associated with the individual galaxies. This term is discussed further in section 7.1.

5.3.2 Single-galaxy fitting

The four group galaxies are initially fitted one at a time, with all other galaxies masked out in order to get parameters as isolated as possible from the rest of the group light. For each fit, a circular mask of radius $2R_\mathrm{e}$[1] is applied around the target galaxy (see Figure 5.2), and a separate mask excludes two bright point sources (a foreground star and a compact background object) located near the group core. The Particle Swarm Optimization (PSO) optimiser within Lenstronomy is used with 200 particles and 200 iterations per galaxy.

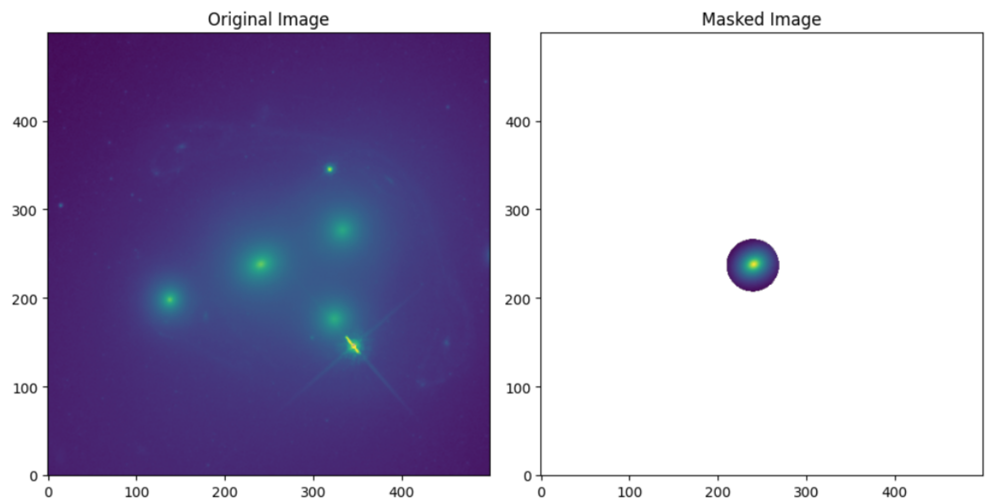

Figure 5.2: Illustration of the mask used for the lens light modeling; single-galaxy fitting. Only the very close vicinity of the fitted galaxy is kept. Scales are in pixels.

An important diagnostic of the single-galaxy fits is the uniform background amplitude. In this mode, the mask prevents contributions from the other three galaxies; the background amplitudes recovered independently for each galaxy are

[1]Initially R_e is unknown so an initial guess is used and this step is repeated enough time so that the value of R_e is well constrained.

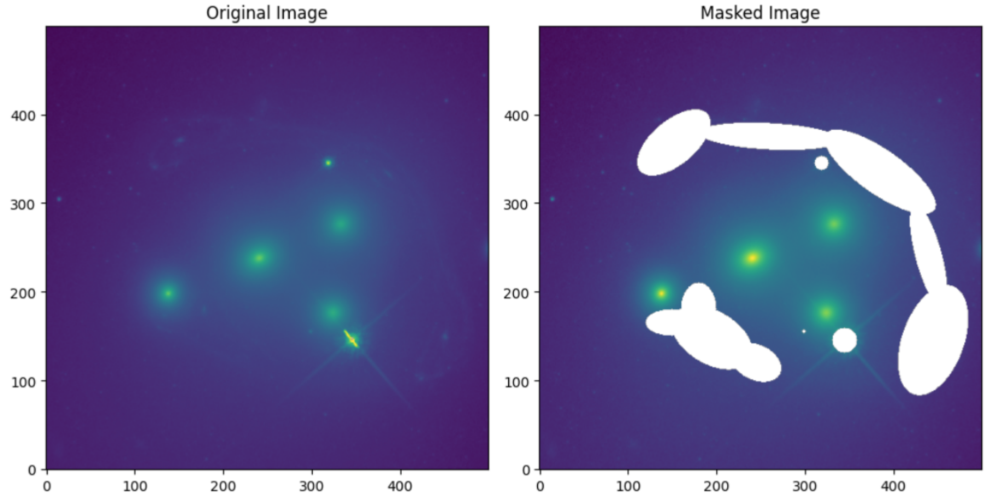

Figure 5.3: Illustration of the mask used for the lens light modeling; simultaneous four-galaxy fitting. The lensed image as well as any foreground stellar sources are masked out. Scales are in pixels.

consistent within $\sim$5% of each other, suggesting a roughly uniform diffuse light contamination across the group core. This diffuse light may originate both from genuine IGL and from the unresolved cumulative flux of other group member galaxies, and cannot be unambiguously attributed to either component from the single-galaxy fits alone.

5.3.3 Simultaneous four-galaxy fitting

In a second step, all four galaxies are fitted simultaneously using the residual image after masking the lensed image regions with elliptical apertures (see Figure 5.3). This approach allows the wings of the profiles to interact self-consistently and avoids the artificial boundary effects introduced by circular masking. The PSO is run with 200 particles and 400 iterations.

5.3.4 Intra-Group Light

Intra-Group Light (IGL) refers to the diffuse stellar emission that does not belong to any individual group galaxy but instead traces the extended stellar envelope of the group gravitational potential, mainly deposited by tidal stripping and merging over cosmic time (Contreras-Santos et al. [2025]). In the context of lens modeling, IGL is analogous to intra-cluster light in cluster-scale lenses and poses a similar challenge: it cannot easily be separated from the wings of the individual galaxy Sérsic profiles using photometry alone, yet its contribution to the lens light model directly affects the accuracy of the lens light subtraction and therefore the quality of the arc residual image used for mass modeling.

In this work, IGL is modeled as a spatially uniform surface brightness component added to the lens light model. While this is clearly a simplification of what is likely a morphologically complex, asymmetric distribution, it provides a consistent parametric handle on the mean IGL level within the 25″ field of view. This degeneracy motivates a direct comparison between models with and without the IGL component, as described in section 6.1 and section 6.3.

5.4 Mass Modeling using the Conjugate Point method

5.4.1 Rationale and approach

Fitting the lens mass model directly to the full surface brightness of the arcs - that is, finding the mass distribution that best reproduces the observed arc images by mapping them back to a single, coherent source - requires a simultaneously optimised model of the source light. At group scales, where the source structure is complex (section 5.5), this joint optimisation of both the mass model and the source light model is sensitive to the initial conditions. A more robust first step is to use only the positions of compact, identifiable features in the arcs - the so-called conjugate points - as astrometric constraints. Each conjugate point set consists of the sky positions of the same region of the lensed galaxy identified in each image (galaxy core, star forming regions identified based on their location, ...). When the lens mass model is correct, all conjugate points within a set ray-trace back to the same source-plane position. The PSO therefore minimises the source-plane scatter of each conjugate-point set independently. This is a purely geometric optimisation: the mass model is evaluated solely on its ability to map observed image positions back to a common source-plane location, without any assumption about or modeling of the source morphology.

5.4.2 Conjugate point identification

ACO 3827 displays a quadruply-imaged source with four visible arc images distributed around the lensing 4-galaxy group (labeled arcs 1-4 starting at the top-right and counting clock-wise). Conjugate points are identified by visual inspection[2] of the F814W science image after masking of lensing galaxies and the bright foreground sources. The following four groups are defined (illustrated in Figure 5.4):

- **Set 0 (central point):** The centroid of the lensed source emission, visible in all four arc images. This is the most reliable constraint owing to its high surface brightness and visibility in every arc.
- **Set 1 (knot A):** A bright compact knot visible in all four arcs, though with lower positional confidence in arc 4[3].

[2] Using the DS9 software, circles can be places centered on the luminosity peak of the region.

[3] The fact that arc 4 sits in close vicinity to one of the lensing galaxy distorts its signal and it is harder to identify the clear position of the conjugate points (Figure 5.4).

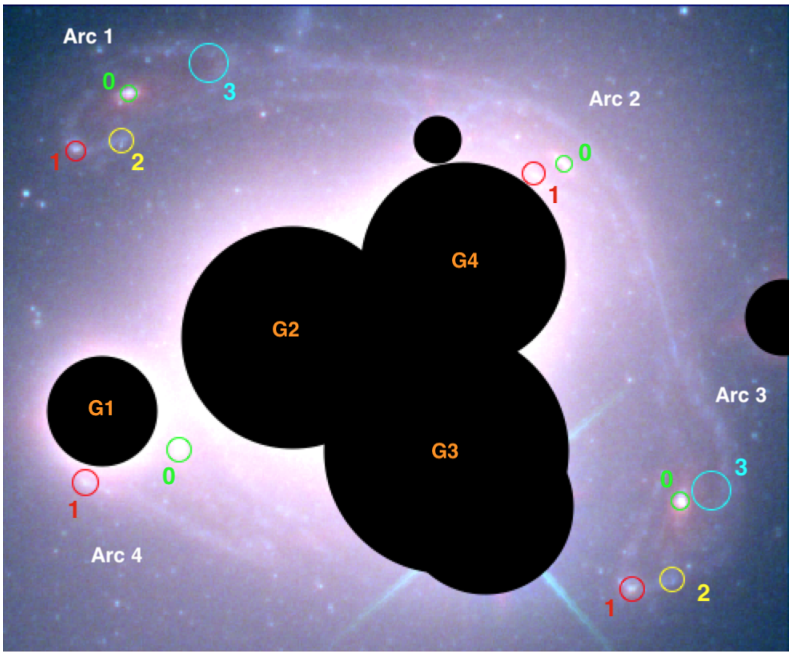

Figure 5.4: HST image of ACO 3827 illustrating the 4 groups of conjugate points identified by visual inspection.

- **Set 2 (knot B):** A secondary knot visible in two arcs only.
- **Set 3 (knot C):** The base of a spiral arm, only visible in two arcs.

Positions are measured in DS9 using sexagesimal RA/Dec coordinates and converted to arcsecond offsets from the center of galaxy G2 (chosen as the coordinate reference because it is the closest galaxy to the centroid of the lens system as well as the brightest of the four). The astrometric uncertainty on each measured position is set to $\sigma_{\text{astro}} = 0.05''$ for the source center and knot A, $\sigma_{\text{astro}} = 0.1''$ for knot B, and $\sigma_{\text{astro}} = 0.2''$ for knot C, reflecting decreasing confidence in the precision of the position of the points. An additional uncertainty of $\sigma = 0.4''$ is applied to the arc 4 measurement of knot A, where the feature is less clearly resolved due to its proximity to galaxy G1. Each component is mapped back in the source plane using the lens equation (Saha et al. [2024]). The modeling is considered as acceptable if the scatter between the mapped position is below $3\sigma_{\text{astro}} = 150$ mas. A summary of the uncertainties and conjugate point positions can be found in Table 5.1.

5.4.3 Mass model parametrisation: 4-SIE model

4 Singular Isothermal Ellipsoid (SIE) are optimized in our model, on for each galaxy. An additional uniform external shear field is added to account for contributions from large-scale structure and any mass outside the modeled region. The lens model list is therefore:

Set	Feature	Image 1 $(\sigma_\alpha, \sigma_\delta)$ [arcsec]	Image 2 $(\sigma_\alpha, \sigma_\delta)$ [arcsec]	Image 3 $(\sigma_\alpha, \sigma_\delta)$ [arcsec]	Image 4 $(\sigma_\alpha, \sigma_\delta)$ [arcsec]
0	Center	(0.05, 0.05)	(0.05, 0.05)	(0.05, 0.05)	(0.05, 0.05)
1	Knot A	(0.05, 0.05)	(0.05, 0.05)	(0.05, 0.05)	(0.4, 0.4)*
2	Knot B	(0.1, 0.1)	(0.1, 0.1)	–	–
3	Knot C	(0.2, 0.2)	(0.2, 0.2)	–	–

Set	Feature	Image 1 $\Delta\alpha$ [arcsec] $\Delta\delta$ [arcsec]	Image 2 $\Delta\alpha$ [arcsec] $\Delta\delta$ [arcsec]	Image 3 $\Delta\alpha$ [arcsec] $\Delta\delta$ [arcsec]	Image 4 $\Delta\alpha$ [arcsec] $\Delta\delta$ [arcsec]
0	Center	+4.443	−7.371	−10.529	+3.095
		+6.615	+4.717	−4.423	−3.037
1	Knot A	+5.869	−6.549	−9.173	+5.627
		+5.070	+4.438	−6.804	−3.912
2	Knot B	+4.629	−10.310	–	–
		+5.326	−6.572	–	–
3	Knot C	+2.278	−11.358	–	–
		+7.424	−4.149	–	–

Table 5.1: *Top:* Astrometric uncertainties assigned to each image set. *Bottom:* Measured positions $(\Delta\alpha, \Delta\delta)$ of each conjugate point, expressed as arcsecond offsets from the reference coordinate $\alpha_0 = 22^h01^m53.361^s$, $\delta_0 = -5956'43.573''$ (J2000). All positions are measured in DS9 and converted to arcsecond offsets from the centre of galaxy G2. The uncertainty σ_{astro} reflects the confidence in the precision of each measured position.

* Enlarged uncertainty applied to the arc 4 position of knot A, where the feature is less clearly resolved due to its proximity to galaxy G1.

$$\{\mathrm{SIE}_1,\ \mathrm{SIE}_2,\ \mathrm{SIE}_3,\ \mathrm{SIE}_4,\ \mathrm{SHEAR}\}. \tag{5.3}$$

For each SIE the ellipticity (e_1, e_2) and center (x_c, y_c) are fixed to the values from the simultaneous Sérsic fit from the lens light model, an assumption was made that these were the most directly constrained structural parameters of each galaxy (this is common in strong gravitational lensing models; Kormann et al. [1994]). Only the Einstein radius θ_{E} of each SIE is left as a free parameter, with a broad uniform prior $\theta_{\mathrm{E}} \in [0.5, 15]''$. The external shear components (γ_1, γ_2) are both free with uniform priors in $[-0.2, 0.2]$, with their reference position fixed to the coordinate origin.

This parametrisation reduces the non-linear optimisation problem to six free parameters (four Einstein radii and two shear components) and is well-suited to the number of independent constraints available from the conjugate points (12 position). The model is implemented in Lenstronomy using the `LENSED_POSITION` point-source class, with one instance per conjugate set.

5.4.4 Mass model parametrisation: 4-SIE + NFW model

To assess whether the four individual galaxy SIE profiles account for the full projected mass of the system, a fifth mass component is added to the model: a `NFW_ELLIPSE_CSE` profile can capture better the possible uncerlying smooth group-scale dark matter halo. This profile is a Core-Softened Ellipsoid (CSE) approximation to the Navarro-Frenk-White (NFW) profile with elliptical projected geometry (cf section 3.3.2), as implemented in Lenstronomy (Oguri [2021]). The halo's parameters are left free with large boundaries to leave more freedom to the model.

The lens model list for this five-component model is:

$$\{\mathrm{SIE}_1,\ \mathrm{SIE}_2,\ \mathrm{SIE}_3,\ \mathrm{SIE}_4,\ \mathrm{SHEAR},\ \mathrm{NFW\_ELLIPSE\_CSE}\}. \tag{5.4}$$

5.4.5 PSO optimisation

Both models are optimised using a PSO algorithm with 200 particles and 400 iterations. The likelihood function combines an image-plane position term and a source-plane scatter penalty, which strongly penalises solutions in which conjugate points within a set do not converge to the same source-plane position. The PSO is initialised with Einstein radii from approximate lensing geometry estimates and converges reliably within the allowed iteration budget.

5.5 Full Surface Brightness Modeling

5.5.1 Overview

Following the conjugate-point analysis, the best-fit mass parameters are used as initial values for a joint optimisation of the lens light, lens mass, and source light. This final step exploits all the morphological information encoded in the arc surface brightness distribution and provides the most precise constraints on the lens mass as well as the morphology of the source. The simultaneous model includes:

1. **Lens light:** Four Sérsic profiles plus a uniform IGL pedestal, fixed to the best-fit values from section 5.3. Fixing the lens light prevents degeneracies between the galaxy profiles and the lensed arc emission.

2. **Lens mass:** Four SIE profiles plus external shear, with positions and ellipticities fixed to the Sérsic fit values and Einstein radii initialised from the conjugate-point PSO result. The Einstein radii are allowed to vary within $\pm 10\%$ of their conjugate-point values.

3. **Source light:** A two-component Sérsic model (described below), with all parameters free within broad physical bounds.

It is important to note that this step could only be done after the use of the conjugate point method to provide a better initial point for the full surface brightness modeling. Indeed, moving straight to this step without the good initial step would give poor results as the optimisation process settles in a local minimum far from optimal results.

5.5.2 Source light parametrisation

The background source at $z_{\rm s} = 1.24$ displays a complex morphology in the lensed images, including a compact bright core and extended arc emission suggesting a galaxy with both a compact stellar nucleus and an extended disk or halo. This is modeled with two Sérsic components:

- **Component 1 (core):** A cuspy Sérsic profile ($n \in [0.5, 8]$, $R_{\rm e} \in [0.005, 3'']$) representing the compact nucleus. The source position is initialised at the mean source-plane position reconstructed from the conjugate-point analysis: $(x_s, y_s) \approx (1.56, 0.03)$ relative to galaxy G2.

- **Component 2 (extended):** A shallower Sérsic profile ($n \in [0.5, 8]$, $R_{\rm e} \in [0.1, \infty]$) representing the outer stellar envelope. It is initialised with a larger effective radius and lower amplitude than the core component and shares the same center.

This parametrisation is physically motivated: the bright knots visible in the arcs are consistent with lensed images of the source core, while the extended blue arc emission traces the outer profile.

Importantly, the source also presents a ring-like structure near the edge of the extended outer envelope. However, the process of representing this structure in Lenstronomy proved to be too complex for the scope of this work. The use of shapelets to model the ring-like structure has been tested but a good model was not reached. We have therefore opted to focus on a combination of 2 Sérsic profiles and leave the modelisation of the ring-like structure to future work.

5.5.3 Mask and fitting procedure

The surface brightness fitting is restricted to the arc regions identified in the lens-light-subtracted residual image, using a mask constructed from three elliptical apertures covering the four arc segments. This avoids biasing the fit by residuals far from the arcs where the lens light subtraction may be imperfect. The PSO is initialised with the conjugate-point mass solution and 300 particles for 400 iterations. A minor residual background level, estimated from the median of source-free regions in the arc mask, is subtracted from the science image prior to fitting to correct for any systematic offset in the lens light model.

Chapter 6

Results

This chapter presents the results of the three-stage analysis pipeline described in chapter 5. We begin with the lens light model and its assessment (section 6.1), then present and compare the conjugate-point mass solutions for the 4-SIE and 4-SIE+NFW configurations (section 6.2), and finally show the results of the full surface brightness modeling (section 6.3).

6.1 Lens Light Model

The best-fit Sérsic parameters from the single-galaxy and simultaneous four-galaxy fits are presented in Table 6.1. The simultaneous fit returns Sérsic indices in the range $n = 3.2$-6.9, consistent with the de Vaucouleurs-like profiles (n = 4) expected for massive early-type galaxies (Graham & Driver [2005]; Kormendy & Ho [2013]). The effective radii range from $1.3''$ to $3.2''$, corresponding to physical half-light radii of roughly 2-6 kpc at $z = 0.099$.

The single-galaxy fits return background amplitudes consistent within $\sim$5% of each other ($\approx$ 114 counts on average), confirming a spatially uniform IGL contribution across the group core. A notable difference between the two fitting strategies is the Sérsic index of G1 ($n = 2.51$ vs $n = 6.89$) and the effective radii of all galaxies, which are systematically larger in the simultaneous fit. This is expected: when only the target galaxy is unmasked, the fit converges on a compact profile with no contribution from the wings of the other three galaxies; when all four are fitted simultaneously, the wings can extend further and the index steepens to describe a more concentrated core. The simultaneous fit returns a global background amplitude of $\approx$ 62 counts, a factor of ~ 1.8 lower than the single-galaxy average, because the extended Sérsic wings of all four components now contribute low-level flux at the group center that was previously absorbed by the background term. The physical interpretation of this discrepancy and its implications for the IGL estimate are discussed in section 7.1.

For the subsequent analysis, the simultaneous four-galaxy parameters are adopted as the lens light model. The larger mask covering the full arc region allows the Sérsic wings to interact self-consistently, yielding a more accurate

Galaxy	R_e [″]	n	e	ϕ [°]	x_c [″]	y_c [″]	A_{BG}
			Single-galaxy fit				
G1	0.742	2.505	0.133	24.1	−5.143	−2.001	110.88
G2	0.742	2.505	0.133	24.1	0.000	0.000	111.69
G3	0.637	1.374	0.031	−43.1	4.166	−3.089	117.23
G4	0.677	1.302	0.029	32.0	4.604	1.920	117.03
			Simultaneous four-galaxy fit				
G1	1.621	6.892	0.039	−28.9	−5.143	−2.002	62.41
G2	1.329	3.489	0.116	27.1	0.000	0.000	
G3	2.839	3.369	0.049	−43.3	4.166	−3.095	
G4	3.210	3.229	0.025	14.4	4.610	1.927	

Table 6.1: Best-fit Sérsic parameters from the single-galaxy fits (each galaxy masked separately) and simultaneous four-galaxy fit. Galaxy centers are given as arcsecond offsets relative to the reference point (galaxy 2 center). The ellipticity $e = \sqrt{e_1^2 + e_2^2}$ and position angle $\phi = \frac{1}{2}\arctan(e_2/e_1)$ are derived from the complex ellipticities. A_{BG} is the uniform background amplitude.

description of the group light distribution at the radii relevant for arc modeling.

Figure 6.1 shows the data image, the best-fit lens light model, and the normalised residual image for the simultaneous four-galaxy fit. The residuals are at the level of a few percent of the galaxy peak flux. The arc emission is clearly visible in the residual image as a ring of positive residuals surrounding the group core, well above the noise level.

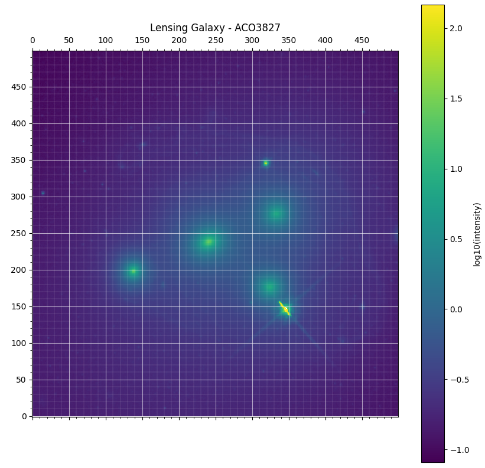

(a) F814W science image

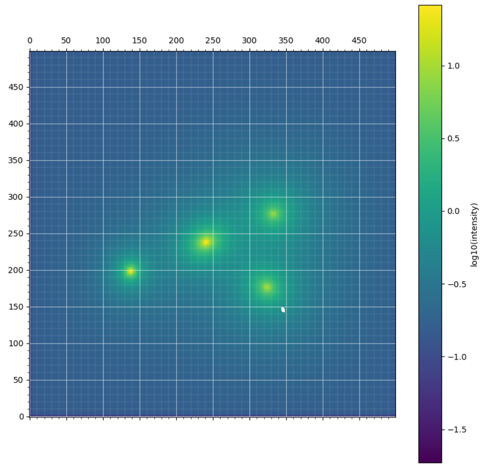

(b) Best-fit lens light model (four Sérsic profiles plus uniform background)

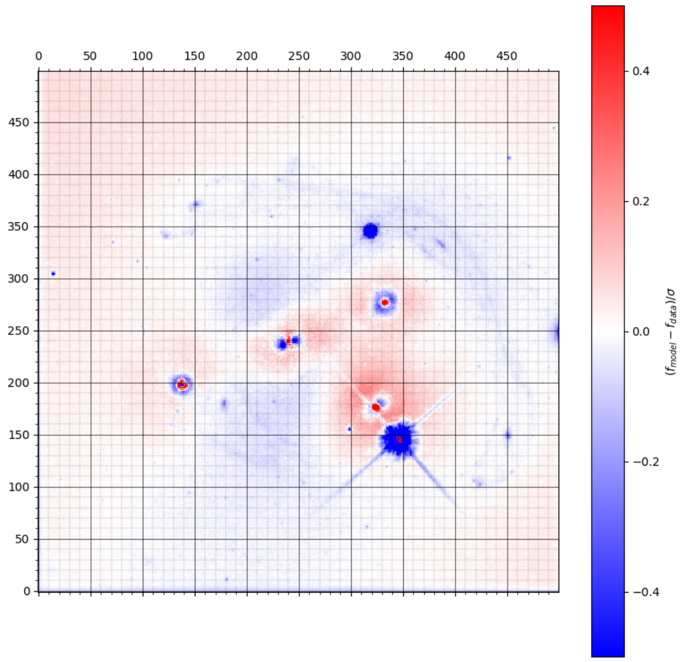

(c) Normalised residual $(I_{\mathrm{data}} - I_{\mathrm{model}})/\sigma$

Figure 6.1: Lens light modeling of ACO 3827. The arc emission from the lensed background source is clearly captured in the residual image.

6.2 Mass Modeling using the Conjugate Point method

Table 6.2 reports the corresponding source-plane scatter per conjugate group, enabling a direct comparison of reconstruction quality between the two configurations. Table 6.3 lists the best-fit SIE Einstein radii from the PSO optimisation for both the 4-SIE and 4-SIE+NFW models.

Set	Feature	N_{img}	4-SIE			4-SIE+NFW		
			σ_{RA} [mas]	σ_{Dec} [mas]	σ_{tot} [mas]	σ_{RA} [mas]	σ_{Dec} [mas]	σ_{tot} [mas]
0	Center	4	41.6	56.6	70.2	27.8	31.1	41.8
1	Knot A	4	96.3	71.4	119.9	24.4	52.7	58.1
2	Knot B	2	5.4	43.8	44.2	35.0	9.4	36.2
3	Knot C	2	40.2	126.7	132.9	15.1	109.0	110.0

Table 6.2: Source-plane scatter per conjugate group after PSO optimisation, for both mass models. The target criterion is $\sigma_{\mathrm{tot}} < 3\,\sigma_{\mathrm{astro}} = 150\,\mathrm{mas}$ for all groups.

Component	Parameter	4-SIE	4-SIE+NFW
G1	θ_{E} [$''$]	1.36	1.39
G2	θ_{E} [$''$]	2.75	2.49
G3	θ_{E} [$''$]	2.01	1.74
G4	θ_{E} [$''$]	2.58	1.47
NFW	r_{s} [$''$]	-	12.63
	κ_{s}	-	1.78
Shear	γ_1	0.074	0.086
	γ_2	-0.125	-0.089

Table 6.3: Best-fit SIE Einstein radii and NFW parameters for both conjugate point models. Galaxy positions and ellipticities are fixed to the lens light model values (Table 6.1).

The 4-SIE model already provides a reasonable reconstruction, with scatter ranging from 44.2 mas (knot B, Set 2) to 132.9 mas (knot C, Set 3). Adding the group-scale NFW halo as a fifth mass component reduces the scatter systematically across all groups, with the most significant improvements for Set 1 (from 119.9 to 58.1 mas, $\sim$52% reduction) and Set 0 (from 70.2 to 41.8 mas, $\sim$40% reduction). Set 3 improves more modestly (from 132.9 to 110.0 mas), while Set 2 is essentially unaffected (44.2 $\rightarrow$ 36.2 mas). The mean scatter reduction across all groups is $\approx$ 35%, achieved with a single additional mass component. This systematic improvement suggests that a non-negligible fraction of the total convergence within the arc region originates from a smooth, extended group-scale halo rather than from the individual galaxy halos alone.

The SIE and NFW components describe physically different objects operating on very different scales - individual galaxy halos of a few kiloparsecs versus a group-scale halo potentially extending to hundreds of kiloparsecs - and their masses cannot be meaningfully added into a single total. We therefore characterise them separately using the most appropriate mass estimator for each.

Galaxy masses. For each SIE component, the natural mass estimator is the total projected mass enclosed within its own Einstein radius,

$$M_{\mathrm{SIE}}(<\theta_{\mathrm{E}}) = \pi\,\Sigma_{\mathrm{cr}}\,\theta^2_{\mathrm{E,\,kpc}}, \tag{6.1}$$

where $\theta_{\mathrm{E,\,kpc}} = \theta_{\mathrm{E}}\,D_{\mathrm{l}}$ is the physical Einstein radius. This quantity is the most robustly constrained by the lensing data. In addition, to compare galaxy masses on equal footing across the two models - which have different individual Einstein radii - we also evaluate all four SIE profiles within the common aperture $\theta_{\mathrm{sys}} = 8''$ ($\approx 15\,\mathrm{kpc}$), which encompasses all observed lensed images. For an SIE, $M(<R) = \pi\,\Sigma_{\mathrm{cr}}\,\theta_{\mathrm{E}}\,R$ grows linearly in R, so this comparison is straightforward. Both sets of masses are listed in Table 6.4, using $\Sigma_{\mathrm{cr}} = 4.94 \times 10^9\,\mathrm{M}_\odot\,\mathrm{kpc}^{-2}$ for $z_{\mathrm{lens}} = 0.099$, $z_{\mathrm{src}} = 1.24$.

Group halo mass: M_{500c}. The NFW halo is characterised by M_{500c}, the total three-dimensional mass enclosed within the radius R_{500c} at which the mean interior mass density equals $500\,\rho_c(z)$, the critical density of the universe at the lens redshift. This is the standard mass estimator for group- and cluster-scale halos and does not depend on an arbitrary aperture choice. Given the lensing parameters κ_s and r_s, the three-dimensional NFW density profile is

$$\rho(r) = \frac{\rho_s}{(r/r_s)(1 + r/r_s)^2}, \qquad \rho_s = \frac{\kappa_s\,\Sigma_{\mathrm{cr}}}{r_s}, \tag{6.2}$$

and R_{500c} is found by solving

$$\frac{M_{\mathrm{NFW}}(<R_{500c})}{\frac{4}{3}\pi R^3_{500c}} = 500\,\rho_c(z_{\mathrm{lens}}). \tag{6.3}$$

With $\rho_c(z = 0.099) = 1.49 \times 10^2\,\mathrm{M}_\odot\,\mathrm{kpc}^{-3}$, the best-fit parameters $\kappa_s = 1.78$ and $r_s = 12.63'' = 23.1\,\mathrm{kpc}$ yield $R_{500c} \approx 787\,\mathrm{kpc}$ and $M_{500c} \approx 1.5 \times 10^{14}\,\mathrm{M}_\odot$. We caution, however, that these values carry large uncertainties: the conjugate-point optimisation constrains only the projected convergence within the arc region ($\lesssim 15\,\mathrm{kpc}$), leaving the 3D NFW parameters κ_s and r_s highly degenerate. The inferred concentration $c_{500} \equiv R_{500c}/r_s \approx 34$ is unphysically high compared with predictions from N-body simulations ($c_{500} \sim$ 3-6 for group-scale halos; Navarro et al. 1996), confirming that M_{500c} cannot be reliably determined from strong-lensing point-image data alone. The reported value should therefore be treated as an upper bound subject to revision once weak-lensing or X-ray constraints are incorporated.

	$M(<\theta_{\mathrm{E},i})$ - individual Einstein radius		$M(<8'')$ - common aperture	
	4-SIE	4-SIE+NFW	4-SIE	4-SIE+NFW
	$[10^{11}\,\mathrm{M}_\odot]$	$[10^{11}\,\mathrm{M}_\odot]$	$[10^{11}\,\mathrm{M}_\odot]$	$[10^{11}\,\mathrm{M}_\odot]$
G1	0.96 (2.5 kpc)	1.00 (2.5 kpc)	5.64	5.77
G2	3.92 (5.0 kpc)	3.22 (4.6 kpc)	11.41	10.34
G3	2.10 (3.7 kpc)	1.57 (3.2 kpc)	8.34	7.22
G4	3.45 (4.7 kpc)	1.12 (2.7 kpc)	10.71	6.10
Total	Not physical		36.11	29.43

NFW group halo	4-SIE+NFW
r_s	$12.63'' \approx 23\,\mathrm{kpc}$
R_{500c}	$\approx 787\,\mathrm{kpc}$
M_{500c}	$\approx 1.5\times10^{14}\,\mathrm{M}_\odot$ (poorly constrained; see text)

Table 6.4: Projected SIE masses for both models. Left block: mass within each galaxy's individual Einstein radius $\theta_{\mathrm{E},i}$ (physical half-mass radius in kpc given in parentheses). Right block: mass within the common system aperture $\theta_{\mathrm{sys}} = 8''$ ($\approx 15\,\mathrm{kpc}$) for direct model comparison. All masses in units of $10^{11}\,\mathrm{M}_\odot$. The NFW group halo is characterised separately by M_{500c} (see text).

Model 1 (4-SIE+NFW, without external shear)					
Set	Feature	x_s [″]	y_s [″]	Δx_s [″]	Δy_s [″]
0	Source center	+1.584	+0.049	0	0
1	Knot A	+1.222	−0.643	−0.361	−0.692
2	Knot B	+1.819	−0.809	+0.236	−0.858
3	Knot C	+2.221	+0.042	+0.637	−0.008

Model 2 (5-SIE+NFW, with external shear)					
Set	Feature	x_s [″]	y_s [″]	Δx_s [″]	Δy_s [″]
0	Source center	+1.486	+0.000	0	0
1	Knot A	+1.169	−0.764	−0.317	−0.764
2	Knot B	+1.725	−0.925	+0.239	−0.925
3	Knot C	+2.040	+0.060	+0.554	+0.060

Table 6.5: Mean source-plane positions of the four conjugate groups for both lens models. Model 1 uses 4 SIEs+NFW without external shear; Model 2 adds a fifth SIE component acting as external shear. Positions are arcsecond offsets from the G2 centre. Δx_s and Δy_s are offsets relative to Set 0.

Within the common aperture of $8''$, the total SIE galaxy mass decreases by $\approx 18\%$ when the NFW halo is added ($36.1 \rightarrow 29.4\times10^{11}\,\mathrm{M}_\odot$), with G4 showing the largest individual reduction ($10.7 \rightarrow 6.1\times10^{11}\,\mathrm{M}_\odot$, -43%) and G1 essentially unchanged. This mass transfer from the galaxy-scale profiles to the group-scale halo is discussed further in subsection 7.2.2.

Mean source-plane positions of the four conjugate groups, derived from both lens models, are listed in Table 6.5. In Model 1 (4-SIE+NFW, without external shear), the source center lies at $(x_s, y_s) \approx (1.58, +0.05)''$ relative to G2, while in Model 2 (5-SIE+NFW, with an additional SIE acting as external shear) it lies at $(x_s, y_s) \approx (1.49, 0.00)''$. The two models yield consistent source-plane geometries, with knot separations from Set 0 agreeing to within $\sim 0.1''$ ($\sim$ 1 kpc). The angular separation between the source center (Set 0) and Knot A (Set 1) is $\approx 0.78''$-$0.83''$, corresponding to a physical separation of $\approx$ 6.3-6.7 kpc at $z_s = 1.24$, comparable to the scale of a large spiral arm.

6.3 Full Surface Brightness Reconstruction

The full joint optimisation described in section 5.5 is performed for three progressively richer source and mass configurations.

Model 1 couples a single-component Sérsic source (compact core only) to the 4-SIE conjugate-point mass solution.

Model 2 retains the same mass parametrisation but extends the source to a two-component Sérsic model (core + extended envelope).

Model 3 adds the group-scale NFW halo as a fifth mass component (4-SIE+NFW) while keeping the two-component source of Model 2. The three models are presented in order of increasing complexity; for each one, the reconstructed source morphology in the source plane and the observed-reconstructed-residual collage in the image plane are shown.

6.3.1 Model 1: Single Sérsic source, 4-SIE mass

Figure 6.2 shows the reconstructed source morphology for Model 1, and Figure 6.3 shows the corresponding image-plane fit. In the source plane, the optimiser converges to a compact, centrally concentrated brightness distribution. The recovered source position, $(x_s, y_s) \approx (1.56, 0.03)''$ relative to G2, is consistent with the mean position inferred from the conjugate-point analysis (Table 6.5). However, the single-component model accounts only for the bright central peak of the source galaxy; the arc centre labelled *arc centre* in Figure 6.2 sits precisely on the primary peak, but the discrete star-forming knots A, B, and C - which lie at projected separations of ~ 0.6-$0.9''$ from the source centre in the source plane - remain largely unreproduced. The 4-SIE mass model, initialised from the conjugate-point solution but constrained here only by the surface brightness of the arc, adjusts its Einstein radii to minimise the global χ^2 but cannot simultaneously reproduce the compact core and the extended arc emission with a single source component.

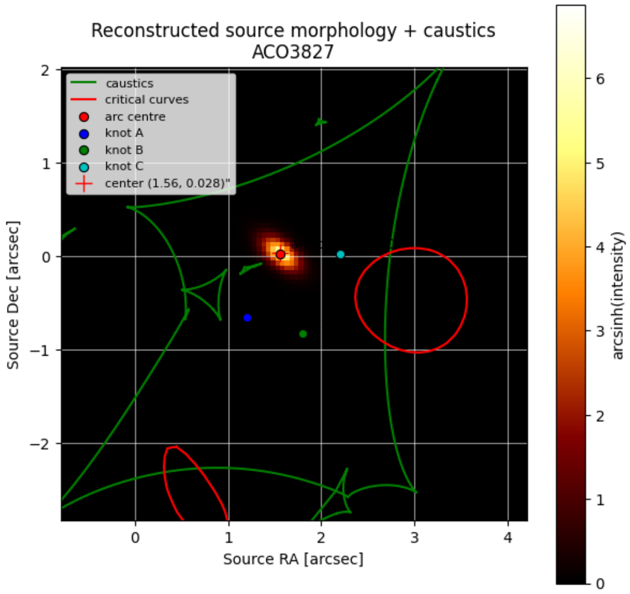

Figure 6.2: Reconstructed source morphology and caustics for Model 1 (single Sérsic core, 4-SIE mass). The colour scale is arcsinh-stretched intensity in the source plane. Coloured markers indicate the source-plane positions of the arc centre (red), knot A (blue), knot B (green), and knot C (cyan) as inferred from the conjugate-point analysis. The pink cross marks the lens-model source-plane centre. The single-component model concentrates all emission at the arc centre and cannot account for the off-centre knots.

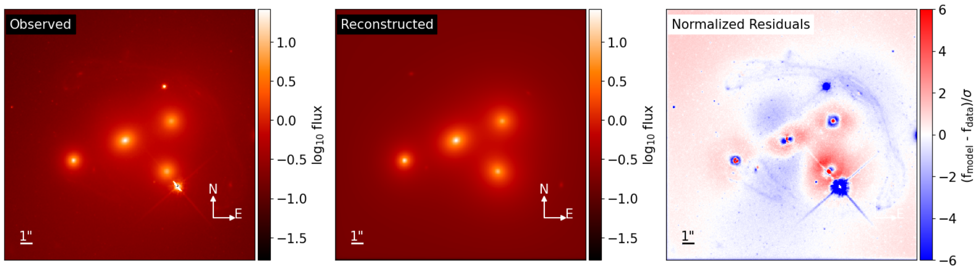

Figure 6.3: Image-plane reconstruction for Model 1. *Left:* F814W science image. *Centre:* Best-fit model (lens light + lensed source). *Right:* Normalised residuals $(f_{\text{model}} - f_{\text{data}})/\sigma$.

6.3.2 Model 2: Two-component Sérsic source, 4-SIE mass

Model 2 introduces a second, extended Sérsic component in the source plane while retaining the 4-SIE mass parametrisation. The source-plane reconstruction is shown in Figure 6.4 and the image-plane fit in Figure 6.5.

The addition of an extended envelope component produces a qualitatively different source morphology: the outer Sérsic profile creates a broader, shallower intensity distribution whose caustic-mapped images contribute diffuse arc flux between the discrete knots. The reconstructed source now exhibits a more extended profile, and the contribution of the extended component is visible as the gentler gradient of the background in Figure 6.4 relative to the sharply peaked Model 1 result. The image-plane residuals improve noticeably in the inter-knot arc regions.

However, Model 2 remains systematically limited by the mass parametrisation. Without a group-scale smooth halo, the four SIE components must account for all convergence in the arc region, including the contribution of any diffuse group dark matter. The optimiser adjusts the individual Einstein radii - in particular inflating the Einstein radius of G4 (which lies closest to the image arcs) - in an attempt to reproduce the extended arc emission. This leads to an over-estimated Einstein radius for G4 and, correspondingly, to inaccurate geometry. In this case, this leads to a degeneracy of the large sersic extending far beyond the identified conjugate points representing star-forming regions on the edge of the source galaxy.

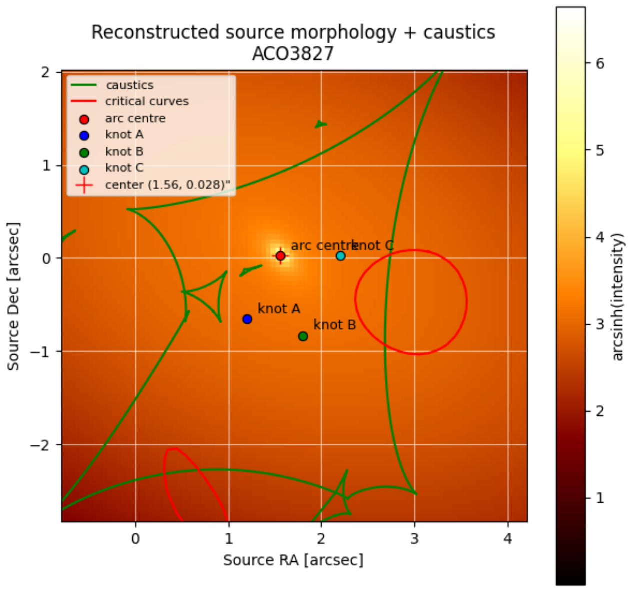

Figure 6.4: Reconstructed source morphology and caustics for Model 2 (two-component Sérsic, 4-SIE mass). The extended Sérsic component produces a broader intensity distribution visible as a uniform background relative to Model 1.

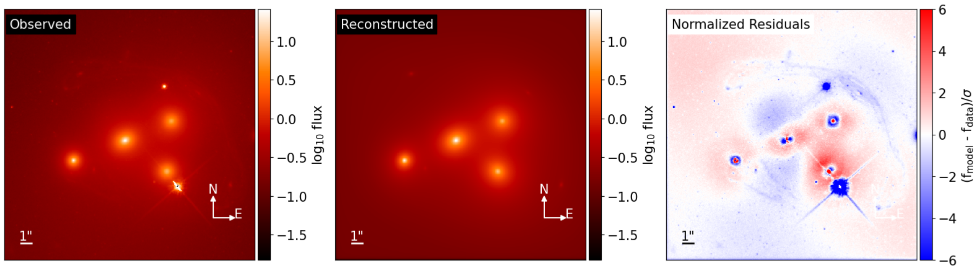

Figure 6.5: Image-plane reconstruction for Model 2. The inter-arc diffuse emission improves relative to Model 1, but residuals at the position of the peripheral knots A and C persist, reflecting the inability of the 4-SIE mass model alone to correctly reproduce the full caustic geometry.

6.3.3 Model 3: Two-component Sérsic source, 4-SIE+NFW mass

Model 3 combines the two-component Sérsic source of Model 2 with the full 4-SIE+NFW mass model. The NFW group halo parameters are initialised from the conjugate-point best-fit values ($\kappa_s = 1.78$, $r_s = 12.63''$; see Table 6.3) and allowed to vary within broad bounds during the surface brightness optimisation. The source-plane reconstruction is shown in Figure 6.6 and the image-plane fit in Figure 6.7.

The inclusion of the group-scale NFW halo seems to produce an improved reconstruction. In the source plane (Figure 6.6), the caustic geometry is now more compact and better centred on the emission peak, reflecting the redistribution of smooth convergence from the over-inflated galaxy-scale SIE profiles to the group halo. Critically, the peripheral conjugate knots - knot A (Set 1) and knot C (Set 3), which lie at the edges of the source galaxy and correspond to off-nuclear, star-forming regions - now fall closer to the Sérsic profile boundary in the expected configuration. The resulting lensed images of these knots are better mapped to the observed arc positions, and the image-plane residuals (Figure 6.7) are significantly reduced across the full arc region.

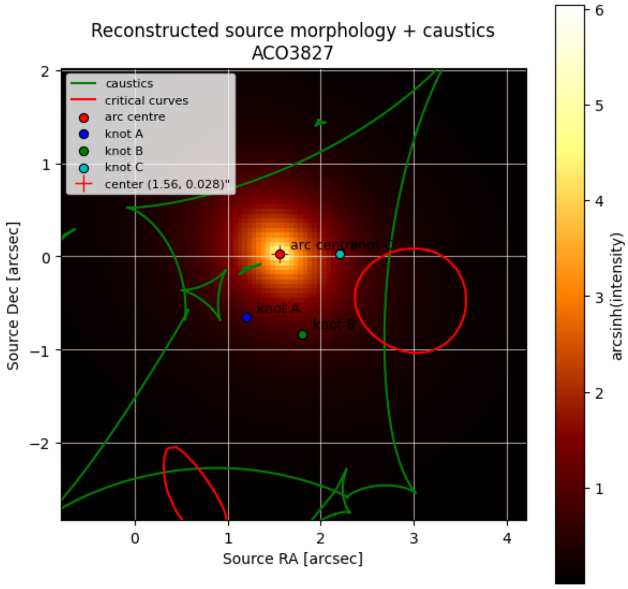

Figure 6.6: Reconstructed source morphology and caustics for Model 3 (two-component Sérsic, 4-SIE+NFW mass). The source now displays a compact bright core surrounded by a more extended envelope, consistent with the morphology of a star-forming galaxy at $z \sim 1.2$.

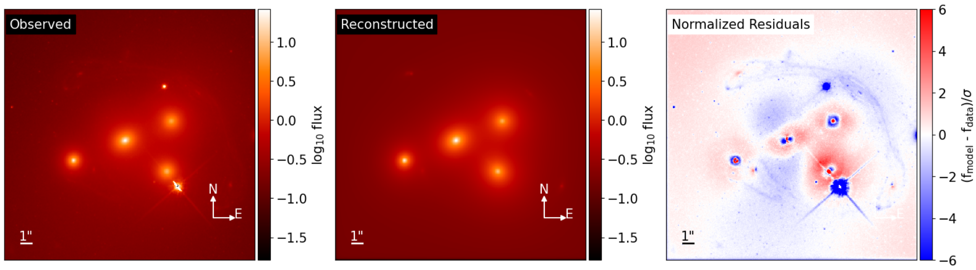

Figure 6.7: Image-plane reconstruction for Model 3. The full arc morphology is reproduced more faithfully than in Models 1 and 2, with normalised residuals reduced to $|\Delta| \lesssim 3\sigma$ across most of the arc mask. The remaining excesses are localised to the bright knot cores (PSF-limited) and to the diffraction spike of a nearby star.

6.3.4 Summary of model comparison

Looking solely at the residuals maps, the three models do not show a clear improvement hierarchy. This is due to the fact that the residual maps are dominated by the lens light model residuals. The clear improvement comes when looking at the source-plane morphology. Model 1 demonstrates that a single Sérsic profile capturing only the compact core is insufficient: the 4-SIE mass model, unconstrained by the extended arc morphology, cannot map the peripheral haloes to their observed image positions. Model 2 improves the inter-arc diffuse emission by adding an extended source component, but the 4-SIE mass parametrisation remains under-constrained without a group-scale halo, causing individual Einstein radii - particularly that of G4 - to be artificially inflated. Model 3 resolves both limitations simultaneously: the NFW group halo redistributes smooth convergence away from the galaxy-scale profiles, the caustic network reshapes to encompass the peripheral star-forming knots, and the two-component source model captures both the compact core and the extended emission. The progression from Model 1 to Model 3 illustrates the importance of simultaneously fitting a physically complete mass model and a morphologically adequate source model, and confirms that a group-scale smooth halo is required not only by the conjugate-point scatter (section 6.2) but also by the full surface brightness distribution of the arc.

Chapter 7

Discussion

The results presented in chapter 6 constitute a self-consistent strong-lensing characterisation of ACO 3827, one of the few well-resolved group-scale lens systems available for detailed analysis. In this chapter we interpret those results in the context of the theoretical framework introduced in chapter 2 and chapter 3. We discuss the lens light model and its implications for the intra-group light (section 7.1), the properties of the mass distribution inferred from conjugate-point modeling (section 7.2), the characterisation of ACO 3827 as a group-scale lens intermediate between galaxy- and cluster-scale systems (section 7.3), a comparison with the published cluster-scale lensing analysis of Chen et al. [2020] (section 7.4), and the principal limitations and systematic uncertainties of the analysis (section 7.5).

7.1 Intra-Group Light and Lens Light Modeling

The simultaneous four-galaxy Sérsic fit returns a uniform background amplitude of ≈ 62 counts, a factor of ~ 1.8 lower than the average of the four independent single-galaxy fits (≈ 114 counts). This discrepancy has a straightforward physical explanation: in the simultaneous fit the extended Sérsic wings of all four components contribute low-level flux at the group centre, partially accounting for the smooth light that the single-galaxy fits absorb entirely into the background term. The two fitting strategies therefore bracket the true IGL contribution rather than providing independent measurements of it.

Whether the true IGL level is closer to 62 or 114 counts has a practical consequence for the arc residuals used in Stage 3. A higher background leaves a positive pedestal beneath the arcs after galaxy subtraction, boosting the inferred arc flux and the normalisation of the source model; a lower background produces a cleaner residual but may leave genuine IGL emission unaccounted for, redistributing it into the Sérsic wings. For the mass analysis this is a second-order concern, since the conjugate-point constraints in Stage 2 depend only on image positions and are insensitive to the surface brightness calibration. For the source-plane reconstruction in Stage 3, however, the choice of background level enters directly into the normalisation of the arc flux. This is identified as a systematic uncertainty in section 7.5.

More broadly, the factor of $\sim$1.8 difference in background amplitude between the two strategies illustrates the fundamental difficulty of separating IGL from the extended wings of individual group member profiles. This challenge is well documented in the intra-cluster light literature for cluster-scale systems (e.g., Montes [2022]) and echoes similar degeneracies found in group-scale studies. It underscores the need for physically motivated IGL models - rather than uniform background terms - in future analyses of group-scale lenses, particularly as wide-field surveys such as Euclid and Rubin provide shallower but more numerous group-lens samples.

The simultaneous fit is adopted for all subsequent analysis because its larger arc mask allows the Sérsic wings to interact self-consistently, providing a more accurate description of the group light distribution at the radii relevant for arc modeling.

7.2 Dark Matter Halo Properties

7.2.1 Improvement from the group-scale halo

The central quantitative result of the conjugate-point analysis is the systematic improvement in source-plane scatter when the NFW halo is added as a fifth mass component. The mean scatter across all conjugate groups decreases by $\approx 35\%$ - from a range of 44-133 mas in the 4-SIE model to 36-110 mas in the 4-SIE+NFW model - with all groups remaining well within the $3\,\sigma_{\text{astro}} = 150$ mas threshold. This improvement, achieved by introducing a single additional mass component, indicates that the four galaxy-scale SIE profiles alone do not fully account for the mass distribution within the lensing region.

The physical interpretation is straightforward: some fraction of the total convergence within the arc region originates from a smooth, extended component associated with the group dark matter halo rather than with any individual galaxy. We describe the group-scale smooth and large potential with an NFW profile. They are particularly well-suited for such large-scale halo description as reported multiple time from simulation of collisionless particles (e.g. Navarro et al. [1996]) such as dark matter.

The improvement is not uniform across conjugate groups. The largest gains are in Set 1 (knot A, $\sim$52% improved rms) and Set 0 (the source centre, $\sim$40% improved rms), while Set 3 (knot C) improves more modestly ($\sim$17%) and Set 2 (knot B) is nearly unaffected. This pattern is consistent with the geometry of the NFW halo: groups whose images span a larger range of azimuths around the lens centre are more sensitive to a smooth, azimuthally symmetric component, while pairs of images on similar radii (Set 2 has only two images) impose weaker constraints on a circularly symmetric halo.

7.2.2 Mass redistribution between models

Because the SIE galaxy profiles and the NFW group halo describe objects of fundamentally different physical scales - individual galaxy halos confined to a few kiloparsecs versus a group halo extending to hundreds of kiloparsecs - their masses cannot be combined into a single total. Instead, the two components must be characterised separately: the galaxies by their SIE Einstein-radius masses (or a common-aperture equivalent), and the group halo by M_{500c}.

The addition of the NFW halo triggers a clear transfer of mass away from the galaxy-scale SIE profiles. Within the common aperture of $8''$ (≈ 15 kpc), the total SIE galaxy mass decreases from 36.1 to $29.4 \times 10^{11}\,\mathrm{M}_\odot$ (-18%). The effect is strongest for G4, whose Einstein-radius mass falls from 3.45 to $1.12 \times 10^{11}\,\mathrm{M}_\odot$ (-68%, corresponding to a change in Einstein radius from $2.58''$ to $1.47''$), and smallest for G1, which is essentially unchanged. This is physically expected: in the 4-SIE model, the outer wings of the galaxy profiles - particularly that of G4, which lies closest to the group centre - absorb smooth convergence that is more naturally attributed to a group-scale halo; once the NFW component is present, G4's SIE contracts to describe only the galaxy's own gravitational potential. This degeneracy between galaxy-scale and group-scale mass is a well-known challenge in multi-component lens modeling [Limousin et al., 2022] and is discussed further in section 7.5.

The group halo is characterised by $M_{500c} \approx 1.5 \times 10^{14}\,\mathrm{M}_\odot$ at $R_{500c} \approx 787$ kpc, placing it at the high end of the galaxy-group to poor-cluster transition regime. As discussed in section 6.2, this value carries large systematic uncertainties due to the limited radial range probed by the strong-lensing constraints alone; it should be understood as an order-of-magnitude indicator rather than a precise measurement.

7.2.3 Connection to the stellar-to-halo mass relation

Without an independent estimate of the stellar mass of the group galaxies from SED fitting or spectroscopy, a quantitative statement about the dark matter fraction is not possible from this analysis alone. However, a qualitative comparison with the SHMR is instructive. The indicative $M_{500c} \approx 1.5 \times 10^{14}\,\mathrm{M}_\odot$ places the system at the high end of the galaxy-group regime. At this halo mass scale, the SHMR predicts a stellar-to-halo mass ratio of $M_\star/M_{500c} \sim 0.01$-$0.02$ [Behroozi et al., 2013], implying that the combined stellar mass of all group galaxies is only ~ 1-2% of the total halo mass - consistent with the picture that dark matter strongly dominates the mass budget of ACO 3827 at the group scale. A full decomposition between stellar and dark matter is deferred to a follow-up analysis once stellar mass estimates from SED fitting are available.

7.2.4 Source-plane morphology

The source-plane positions of the four conjugate groups, derived from the 4-SIE+NFW model, reveal a spatially extended background source. The angular separation between the source centre (Set 0) and knot A (Set 1) is $\approx 0.75''$ in the source plane, corresponding to a physical projected separation of ≈ 6.2 kpc at $z_s = 1.24$. The remaining knots (B and C) lie at comparable projected distances from the source centre, spanning a source-plane extent of $\sim 1''$ (≈ 8.3 kpc).

This spatial structure - a compact central region (Set 0) surrounded by discrete knots at several kiloparsec separations - is consistent with several physical scenarios at $z \sim 1.2$: a clumpy star-forming disk with active knots of star formation at the end of cosmic noon, a compact starburst nucleus embedded in an irregular envelope, or a minor merger involving a close companion. The reconstructed source-plane geometry provides the most direct handle on these scenarios. Set 1 lies at $\approx$ 0.78-0.83 arcsec from Set 0 ($\approx$ 6.3-6.7 kpc), Set 2 at $\approx$ 0.89-0.96 arcsec ($\approx$ 7.2-7.7 kpc), and Set 3 at $\approx$ 0.56-0.64 arcsec ($\approx$ 4.5-5.2 kpc), where the ranges reflect the two lens models (with and without SIE external shear). These separations, of order a few kpc, are typical of large spiral arm offsets or companion nuclei in interacting systems, and are broadly consistent across both models. Distinguishing between these scenarios requires a resolved spectroscopic analysis of the source, which is beyond the scope of this work.

7.2.5 Source morphology from full surface brightness reconstruction

The three surface brightness models presented in section 6.3 provide complementary insights into the physical structure of the $z_s = 1.24$ source galaxy and into the requirements on the lens mass model.

Degeneracy between source complexity and mass model. The failure of Model 1 (single Sérsic, 4-SIE) to reproduce the peripheral arc emission illustrates a fundamental problem that arises when the source model is too restrictive. With only a compact core available in the source plane, the optimiser compensates by distorting the lens mass - inflating the galaxy-scale Einstein radii or adjusting the shear - in an attempt to stretch the single-component source image across the observed arc. This produces systematically biased Einstein radii and a geometry that cannot simultaneously map the central peak and the extended halo or the source galaxy to their observed image positions.

The role of the group-scale halo in the caustic geometry. The comparison between Models 2 and 3 isolates the effect of the group-scale NFW halo on the caustic network. In Model 2, the 4-SIE-only mass model concentrates all smooth convergence in the four galaxy-scale profiles. The Einstein radius of G4 - the galaxy lying closest to the arc images and therefore most degenerate with a group-scale halo - is over-estimated by the optimiser, deforming the caustic in a way that pushes the peripheral conjugate points (knots A and C) outside the caustic boundary. These knots correspond to star-forming regions at the periphery of the source galaxy; their characteristic blue colour and compact morphology in the arc suggest they are active star-forming regions, as expected for a massive disk galaxy approaching the end of cosmic noon at $z \sim 1.2$ (Genzel et al. [2011]; Swinbank et al. [2012]).

Adding the NFW halo in Model 3 corrects this pathology. The group halo absorbs the smooth convergence that was artificially attributed to G4, contracting its Einstein radius to a physically plausible value and relaxing the caustic geometry.

Physical picture of the source galaxy. The two-component Sérsic model recovered in Model 3 - a cuspy central nucleus and a shallower extended envelope - is consistent with the morphology commonly observed in massive star-forming galaxies at $z \sim$ 1-1.5. The compact core likely corresponds to a dense stellar nucleus or a compact starburst, while the extended component traces the diffuse stellar disk or irregular envelope. The fact that the peripheral knots (A, B, C) lie at projected separations of $\sim$6-8 kpc from the source centre in the source plane (Table 6.5) is broadly consistent with the size of an actively star-forming disk at these redshifts. That these knots are resolved as distinct conjugate sets in the arc rather than as a smooth gradient further suggests that the star formation is clumpy and episodic rather than uniformly distributed, a characteristic frequently reported for high-redshift star-forming galaxies observed at high angular resolution [Swinbank et al., 2012].

Remaining residuals and future improvements. Despite the clear improvement of Model 3 over its predecessors, non-negligible residuals remain at the positions of the bright knot cores. These are likely dominated by two effects: (i) sub-pixel centroiding errors in the PSF model, which propagate to sharp residuals at the centres of the lensed images of the compact core, and (ii) the intrinsic limitation of a parametric Sérsic source, which cannot reproduce the irregular brightness distribution of a clumpy, star-forming galaxy. A more flexible source parametrisation - such as polar shapelets or a pixelated source grid on a regularised adaptive mesh - would allow the clumpy structure of knots A, B, and C to be modeled explicitly and would likely reduce the knot-core residuals to the noise level. This is identified as the primary target for a future, more complete analysis. The mass model degeneracy discussed above - in particular the dependence of the caustic geometry on the NFW halo parameters, whose constraints from strong lensing alone are limited to the projected convergence within the arc region - also motivates the inclusion of weak-lensing or X-ray data to anchor the group halo mass scale independently.

7.3 The Intermediate Mass Scale

ACO 3827 occupies the group-to-cluster transition regime, with a multi-galaxy lensing configuration that is qualitatively different from both isolated galaxy-scale lenses (single Einstein radius $\sim$1-3$''$, dominated by a single object) and massive cluster lenses (Einstein radii $\sim$30-60$''$, dominated by a single BCG and a smooth cluster halo).

In the 4-SIE model, the four individual Einstein radii span 1.36$''$-2.75$''$, with no single galaxy dominating the mass budget. The most massive galaxy is G2 ($\theta_{\rm E} = 2.75''$ in the 4-SIE model, 2.49$''$ in the 4-SIE+NFW model), but its Einstein-radius mass ($3.2\text{-}3.9\times10^{11}\,\mathrm{M}_\odot$) accounts for only $\sim$38-46% of the total four-galaxy Einstein-radius mass. This configuration - in which several galaxies of comparable mass jointly produce the group-scale arc - is the observational hallmark of the intermediate mass regime [Limousin et al., 2009; Thanjavur et al., 2010; Stark et al., 2013].

The addition of the group-scale NFW halo shifts the interpretation toward the group regime. The indicative $M_{500c} \approx 1.5 \times 10^{14}\,\mathrm{M}_\odot$ at $R_{500c} \approx 787$ kpc contrasts with the total SIE galaxy mass of only $\approx 6.9\times10^{11}\,\mathrm{M}_\odot$ summed within individual Einstein radii - objects of entirely different scales, which should not be directly compared but which together illustrate that the group dark matter halo, rather than the summed individual galaxy halos, carries the dominant contribution to the lensing potential at group scales. This is the expected behaviour for a system transitioning from the galaxy-group to galaxy-cluster regime, and is consistent with the expectations of the SHMR (subsection 7.2.3).

Compared to the SL2S and CASSOWARY group-scale lens samples [Limousin et al., 2009; Stark et al., 2013], ACO 3827 has more clearly resolved multiple images and a more complete arc morphology than most group-scale lenses, making it an unusually well-constrained system for its mass scale. Its proximity ($z_{\rm lens} = 0.099$) and the availability of deep HST imaging make it a particularly valuable benchmark for group-scale lensing methodology.

7.4 Comparison with Chen et al. [2020]

The most directly relevant published analysis of this same system is that of Chen et al. [2020], who performed a detailed multi-component strong-lensing analysis of the galaxy cluster Abell 3827 (hereafter ACO 3827) using *HST* F336W, F606W, F814W, and F160W imaging together with *Chandra* X-ray data. Although both works model the same lensed background galaxy ($z_s = 1.24$) through the same group of four dominant early-type galaxies (denoted G1-G4 in both papers), several important differences in system, data, and methodology need to be borne in mind when comparing the results.

Modeling approach. Chen et al. construct six lens models using the free-form code WSLAP+ and the parametric code glafic, with between one and seven mass components, and constrain them with 39 multiply-lensed knots corresponding to 9 distinct features in the background galaxy. Our analysis uses the parametric Lenstronomy code with either four or five components, constrained by the positions of four conjugate sets identified in the arc. The richer constraint set of

Chen et al. - made possible by their multi-band *HST* data spanning UV to near-IR - provides tighter constraints on the lens model, particularly on the orientation and ellipticity of the cluster-scale halo.

Cluster-scale halo vs group-scale halo. The central result of Chen et al. is that a smooth, cluster-scale dark matter halo (modeled as a generalised NFW profile with best-fit total mass $\sim 6\times10^{14}\,\mathrm{M}_\odot$ and ellipticity $\epsilon = 0.46$) is required to reproduce the Einstein ring, and that the position angle of this halo aligns with that of the intracluster light (Intra-Cluster Light (ICL)), indicating that the ICL traces the large-scale gravitational potential. In contrast, our group-scale NFW halo operates at a much smaller mass scale appropriate for a galaxy group rather than a massive cluster: the NFW parameters inferred from the conjugate-point fit imply a system mass of the order $\sim 10^{14}\,\mathrm{M}_\odot$, consistent with the rich group regime (cluster-scale haloes typically reach $5\times10^{14}\,\mathrm{M}_\odot$-$10^{15}\,\mathrm{M}_\odot$; Pratt et al. [2019]). The two analyses are therefore probing the same lensing configuration from different perspectives - cluster-scale versus group-scale - and the comparison highlights the importance of an accurate lens redshift in distinguishing these two regimes.

Total projected mass within the Einstein ring. Chen et al. report a total projected lensing mass within the $\sim 10''$ Einstein ring of $\approx 4.5\times10^{12}\,\mathrm{M}_\odot$ for their best parametric model (their Model 3), dominated by the cluster-scale gNFW halo. Within $10''$ our 4-SIE model alone yields a total galaxy mass of $\approx 4.5\times10^{12}\,\mathrm{M}_\odot$, in striking agreement with the Chen et al. total. This is not a coincidence: in both analyses the lensing geometry fixes the total projected mass within the Einstein ring robustly, regardless of how it is partitioned between components. The difference is one of interpretation - Chen et al. attribute this mass primarily to a smooth cluster-scale halo (their $M_{\mathrm{gNFW}} \sim 6\times10^{14}\,\mathrm{M}_\odot$), whereas our 4-SIE model attributes it entirely to the four galaxy-scale profiles. When we add the group-scale NFW halo ($M_{500c} \approx 1.5\times10^{14}\,\mathrm{M}_\odot$, albeit poorly constrained), the galaxy masses within the same aperture decrease by $\approx 18\%$, reflecting the transfer of smooth convergence from the galaxy halos to the group halo. The galaxy-scale component of our model is therefore self-consistent with the published analysis at the level of total projected mass.

Intracluster / intragroup light. Chen et al. find that the ICL of ACO 3827 has a position angle closely aligned with the cluster-scale DM halo (difference $< 15^\circ$), confirming that the ICL traces the large-scale gravitational potential. Our simultaneous Sérsic fitting of the group light does not model the ICL as a separate extended component, which limits our ability to make a directly analogous comparison. However, the factor of $\sim$1.8 discrepancy between our single-galaxy and simultaneous background amplitudes (section 7.1) is consistent with the presence of a diffuse IGL component whose extent and orientation are not captured by the four-galaxy Sérsic model. Future analyses with deeper imaging and an explicit ICL component would allow a similar ICL-halo alignment test to be performed at the group scale.

7.5 Limitations and Systematic Uncertainties

Single system. This analysis is based on a single group-scale lens. While ACO 3827 is an exceptionally well-characterised system, conclusions about the population-level properties of group-scale dark matter haloes - such as the typical concentration, inner slope, or dark matter fraction - cannot be drawn from a single object. The results presented here can however be compared with other future group-scale analyses.

Absence of stellar mass estimate. The decomposition between the stellar mass of the group galaxies and the group dark matter halo requires an independent estimate of $M_\star$ from SED fitting or spectroscopy. Without this, the dark matter fraction cannot be computed. This is the most significant missing piece of the current analysis and is identified as the primary target for follow-up work.

Degeneracy between galaxy and group-scale mass. The decomposition of the total projected mass into four SIE components plus an NFW halo is not unique. The large reduction in G4's Einstein radius between the two models ($2.58'' \to 1.47''$) illustrates that the galaxy profiles and the group halo are partially degenerate: the conjugate-point constraints fix the total projected mass but do not uniquely assign it to individual components. Galaxy centers and ellipticities are fixed to photometric values throughout, introducing an implicit assumption that the total mass distribution - including dark matter - follows the same projected shape as the stellar light at the galaxy scale. A SIE profile is not a dark-matter-free model; it captures the combined mass distribution but does not decompose stellar and dark components, and the assumption that its axis ratio and orientation follow the light is one of geometry rather than a statement about the mass-to-light ratio per se. This choice is a practical necessity given the available constraints, and while the projected shapes of total mass and light are found to be broadly consistent in massive early-type galaxies (Koopmans et al. [2006]), it has not been independently verified for the ACO 3827 group members. More fundamentally, the conjugate-point constraints are insufficient to accurately constrain the group halo centre and ellipticity: a different choice of galaxy ellipticities, or a different centre or axis ratio for the group halo, could produce equally good fits, leaving these parameters poorly determined by the data alone.

IGL background level. As discussed in section 7.1, the factor of ~ 1.8 discrepancy in background amplitude between the single-galaxy and simultaneous four-galaxy fits introduces an uncertainty in the arc surface brightness calibration. This does not affect the mass parameters (both for the galaxies and the

IGL halo) derived in Stage 2 since they are computed using the conjugate point method rather than with a photometric analysis. The discrepancy, however, propagates into the source flux normalisation in Stage 3 and should be treated as a systematic in any photometric analysis of the lensed source.

PSF modeling. The PSF kernel is derived from a single TinyTim model at a fixed focus offset. In-flight focus variations across the HST field of view and over time introduce uncertainties in the PSF profile at the ∼5-10% level in the wings. Given that the arc images are located several arcseconds from the galaxy cores, the PSF wings of the galaxies extend into the arc regions and a mismatch between the true PSF and the TinyTim model could bias the arc flux at the few-percent level.

Mass-Sheet Degeneracy and external convergence. The absolute normalisation of the lens mass model is subject to the MSD: any sheet of uniform mass added to the lens plane leaves the lensing observables unchanged (Gorenstein et al. [1988]). At group scales such as ACO 3827, the MSD is expected to arise primarily from unaccounted mass along the line of sight, captured by an external convergence κ_{ext} from large-scale structure. For a typical line of sight at the redshift of ACO 3827, κ_{ext} is expected to be of order 1-3% (Birrer et al. [2021]), a subdominant uncertainty for the purposes of this analysis.

Source complexity. The source-plane structure recovered from the conjugate-point analysis suggests a spatially extended source with at least four distinct emission knots spanning ∼8.3 kpc. A two-component Sérsic source model, while a reasonable first approximation, cannot fully capture this complexity. A more flexible parametrisation - for example, polar shapelets or a pixelated source on a refined grid - could improve the arc residuals and provide a more physically complete picture of the $z = 1.24$ source galaxy. This is left for future work.

Chapter 8

Conclusion and Future Prospects

8.1 Summary of Results

This thesis has presented a strong gravitational lensing analysis of the galaxy group ACO 3827, a quadruply-imaged system at $z = 0.099$ with a background source at $z_s = 1.24$. The analysis followed a three-stage pipeline implemented in Lenstronomy: parametric lens light modeling to isolate the arc emission, conjugate-point mass optimisation using identifiable arc features as astrometric constraints, and full surface brightness reconstruction fitting the lens mass and source light simultaneously.

It is important to note that the modeling of group-scale systems using Lenstronomy proved to be computationally very demanding and this has limited the extent of the modeling being done in this work. Despite that, some interesting results have been computed and are summarised below for each stage of the modeling process.

Lens light and IGL. By looking at the residual map of the first step of the process, the surface brightness of the four group galaxies (G1-G4) appears to be well described by elliptical Sérsic profiles with indices $n = 3.2$-6.9 and effective radii of $1.3''$-$3.2''$ ($\approx$ 2-6 kpc at $z = 0.099$), consistent with the de Vaucouleurs-like profiles expected for massive early-type galaxies. A systematic comparison between single-galaxy and simultaneous four-galaxy fitting reveals a factor of $\sim$1.8 discrepancy in the inferred uniform IGL background ($\approx$ 114 vs $\approx$ 62 counts). This quantifies the fundamental degeneracy between the IGL level and the extended Sérsic wings of the individual group members, and constitutes the first assessment of IGL modeling uncertainty in ACO 3827 in the context of strong lensing analysis. The simultaneous four-galaxy model is adopted for all subsequent stages, as it allows the Sérsic wings to interact self-consistently across the full arc region.

Conjugate point mass model. Four groups of conjugate points - the source centroid and three distinct morphological knots of the background source - were identified by visual inspection of the residual F814W image. A four-component SIE lens model (one SIE per galaxy plus external shear) reproduces the source-plane positions of all four conjugate groups with a scatter well below the target threshold of 150 mas: the best-constrained group (source centroid, four images) achieves $\sigma_{\rm tot} = 70.2$ mas. The Einstein radii of the four galaxies span 1.36″-2.75″, with no single galaxy dominating the mass budget - a configuration characteristic of the intermediate group-scale regime, qualitatively distinct from both isolated galaxy-scale and cluster-scale lenses.

Group-scale dark matter halo. Adding a fifth mass component in the form of a group-scale NFW halo (the 4-SIE+NFW model) reduces the mean source-plane scatter by ≈35 % across all conjugate groups, from a range of 44-133 mas to 36-110 mas, with the most significant improvement for knot A (≈52 % reduction) and the source centroid (≈40 %). All groups remain within the 150 mas threshold in both models. This systematic improvement, achieved with a single additional free component, provides clear evidence that the four individual galaxy SIE profiles do not fully account for the projected mass within the lensing region, and that a smooth, extended group-scale dark matter component is required by the data. The NFW halo contributes a projected mass of $\approx 29.7 \times 10^{11}\,{\rm M}_\odot$ within 20″, exceeding the summed galaxy SIE mass of $\approx 10.4 \times 10^{11}\,{\rm M}_\odot$ by a factor of ≈2.9, placing the system firmly in a regime where the group dark matter halo provides the majority of the lensing convergence. The inclusion of the NFW halo also redistributes mass among the galaxy components: the Einstein radii of G2, G3, and G4 decrease by 18-67 % relative to the 4-SIE model, illustrating the known degeneracy between galaxy-scale and group-scale mass components in multi-component lens modeling.

Source morphology. The mean source-plane positions of the four conjugate groups, derived from the 4-SIE+NFW model, reveal a spatially extended background source spanning $\sim 1''$ (≈ 8.5 kpc) in the source plane. The angular separation between the source centroid and knot A is $\approx 0.75''$, corresponding to a physical projected separation of ≈ 6.4 kpc at $z_{\rm s} = 1.24$, consistent with the scale of a large spiral arm or close companion nucleus. The two-component Sérsic source model from the full surface brightness reconstruction provides an adequate fit to the arc morphology in the F814W band, recovering a compact nucleus ($R_{\rm e} \approx 0.072''$, $n \approx 3.3$) embedded in an extended stellar envelope ($R_{\rm e} \approx 3''$, $n \approx 0.5$), consistent with a massive star-forming galaxy at cosmic noon.

IGL impact on mass modeling. The IGL treatment has a negligible effect on the astrometric conjugate-point constraints, as these depend only on image positions and not on surface brightness calibration. It does, however, affect the normalisation of the arc flux model in the full surface brightness stage, since the choice of background level determines the pedestal beneath the arcs after galaxy subtraction. This is identified as a systematic uncertainty but does not strongly bias the projected lensing mass, providing useful guidance for future group-scale lensing analyses: careful IGL modeling matters for source reconstruction but is subdominant for mass characterisation.

8.2 Future Prospects

Stellar mass from SED fitting. The most immediate extension of this work is to obtain stellar mass estimates for the four ACO 3827 group galaxies from multi-band SED fitting using all available HST bands (F336W, F606W, F814W, F160W). This would enable a direct computation of the dark matter fraction f_{DM} within the Einstein radius following the decomposition framework described in section 3.5, and a quantitative comparison of ACO 3827 with the SHMR at group scales, where the stellar-to-halo mass ratio is predicted to be $M_{\star}/M_{200} \sim 0.01$-0.02 (Behroozi et al. [2013]). This step will transform the present analysis from a mass characterisation into a full dark matter fraction measurement.

Source morphology with shapelet models. The ring-like arc emission visible in the deepest arc regions of ACO 3827 is not fully captured by the two-Sérsic source parametrisation. A more flexible basis - such as polar shapelets or a pixelated source reconstruction on a refined grid - could better reproduce the source complexity revealed by the four conjugate groups spanning ~ 8.5 kpc in the source plane (subsection 7.2.4). This could help getting a better fit of the full surface brightness in the last step presented in this work, but should not change drastically the mass parameters computed.

Weak lensing and dynamical cross-check. The conjugate-point and surface brightness constraints provide a robust projected mass measurement within $\sim 10''$, but the halo mass M_{200} and concentration c remain degenerate in the absence of additional radial information (section 7.5). Extending the radial mass profile to the virial radius through weak gravitational lensing shear measurements or member galaxy velocity dispersions would break the concentration-mass degeneracy of the NFW halo, provide an independent measurement of M_{200}, and allow a direct comparison with the HMF predictions discussed in subsection 2.1.5. Such data are not currently available for this system, but would be achievable with sufficiently deep wide-field imaging for the lensing shear, or multi-object spectroscopy of confirmed member galaxies for the dynamical constraint. In the era of the *Euclid* Wide Survey, breaking the concentration-mass degeneracy for systems such as this one may become routine.

IGL in a statistical context. The factor of ~ 1.8 discrepancy in the IGL background level between fitting strategies (section 7.1) illustrates the difficulty of separating intra-group light from the extended wings of individual member profiles. Future analyses would benefit from physically motivated IGL models - for example, a smooth two-dimensional surface brightness distribution anchored to the group mass model, or IGL profiles calibrated from hydrodynamical simulations - in place of the uniform background term used here. This is particularly relevant as Euclid and Rubin produce shallower but far more numerous group-lens samples, where a consistent, automated IGL treatment will be essential.

JWST follow-up. The James Webb Space Telescope provides angular resolution of $\approx 0.06''$ in the NIRCam F200W band, a factor of ~ 1.5 finer than the HST ACS/WFC imaging used in this work. For ACO 3827, a deep JWST NIRCam observation would resolve the arc morphology in unprecedented detail, potentially identifying faint additional multiple images, revealing the intrinsic structure of the ring-like emission, and enabling a spatially resolved IGL morphology analysis. Simultaneous JWST/NIRSpec integral-field spectroscopy would provide spatially resolved emission line maps of the $z_s = 1.24$ source galaxy and spectroscopic confirmation of its redshift, closing the remaining observational gaps in the characterisation of this system.

Sample of group-scale lenses from Euclid and Rubin. The work presented in this thesis depends on very time-consuming simulations and models. This has limited the model exploration. However, the methodology developed in this thesis - three-stage pipeline, conjugate-point initialisation, simultaneous IGL modeling - is directly applicable to the statistical samples of group-scale lenses expected from the Euclid space telescope and the Vera C. Rubin Observatory LSST. While existing forecasts focus on galaxy-scale deflectors (Collett [2015]; Ferrami & Wyithe [2024]), the sheer survey volume and depth of these missions can be expected to yield a corresponding increase in the discovery of group-scale systems as well, substantially expanding the known population beyond the few tens of systems currently comprising the SL2S and CASSOWARY samples (Limousin et al. [2009]; Stark et al. [2013]; cf section 3.6). Applying the pipeline to such a sample would provide the first statistical characterisation of dark matter properties - concentration, inner slope, dark matter fraction - across the group mass regime, directly extending the proof-of-concept demonstrated here for ACO 3827. Doing so at scale would however require significant effort to reduce the current human intervention needed at each stage of the pipeline, which we leave as a natural avenue for future work.

Bibliography

Abell, G. O., Corwin, Jr., H. G., & Olowin, R. P., *A Catalog of Rich Clusters of Galaxies*, 1989, ApJS, 70, 1

Alam, S., et al., *The clustering of galaxies in the completed SDSS-III Baryon Oscillation Spectroscopic Survey: cosmological analysis of the DR12 galaxy sample*, 2017, MNRAS, 470, 2617

Barnes, J. E., & Hernquist, L., *Dynamics of interacting galaxies.*, 1992, ARA&A, 30, 705

Bartelmann, M., & Schneider, P., *Weak gravitational lensing*, 2001, Phys. Rep., 340, 291

Behroozi, P. S., Wechsler, R. H., & Conroy, C., *The Average Star Formation Histories of Galaxies in Dark Matter Halos from z = 0-8*, 2013, ApJ, 770, 57

Birrer, S., & Amara, A., *lenstronomy: Multi-purpose gravitational lens modelling software package*, 2018, Physics of the Dark Universe, 22, 189

Birrer, S., et al., *lenstronomy II: A gravitational lensing software ecosystem*, 2021, JOSS, 6, 3283

Blumenthal, G. R., Faber, S. M., Flores, R., & Primack, J. R., *Contraction of Dark Matter Galactic Halos Due to Baryonic Infall*, 1986, ApJ, 301, 27

Blumenthal, G. R., Faber, S. M., Primack, J. R., & Rees, M. J., *Formation of galaxies and large-scale structure with cold dark matter.*, 1984, Nature, 311, 517

Bond, J. R., Kofman, L., & Pogosyan, D., *How filaments of galaxies are woven into the cosmic web*, 1996, Nature, 380, 603

Boselli, A., Fossati, M., & Sun, M., *Ram pressure stripping in high-density environments*, 2022, A&A Rev., 30, 3

Boylan-Kolchin, M., Bullock, J. S., & Kaplinghat, M., *Too big to fail? The puzzling darkness of massive Milky Way subhaloes*, 2011, MNRAS, 415, L40

Bullock, J. S., & Boylan-Kolchin, M., *Small-Scale Challenges to the ΛCDM Paradigm*, 2017, ARA&A, 55, 343

Carrasco, E. R., et al., *Strong Gravitational Lensing by the Super-massive cD Galaxy in Abell 3827*, 2010, ApJ, 715, L160

Chen, M. C., et al., *Geometric Support for Dark Matter by an Unaligned Einstein Ring in A3827*, 2020, ApJ, 898, 81

Clowe, D., et al., *A Direct Empirical Proof of the Existence of Dark Matter*, 2006, ApJ, 648, L109

Collett, T. E., *The Population of Galaxy-Galaxy Strong Lenses in Forthcoming Optical Imaging Surveys*, 2015, ApJ, 811, 20

Contreras-Santos, A., et al., *The origin of the intracluster light in The Three Hundred simulations*, 2025, A&A, 703, A85

Croton, D. J., et al., *The many lives of active galactic nuclei: cooling flows, black holes and the luminosities and colours of galaxies*, 2006, MNRAS, 365, 11

Davis, M., Efstathiou, G., Frenk, C. S., & White, S. D. M., *The evolution of large-scale structure in a universe dominated by cold dark matter*, 1985, ApJ, 292, 371

Dressler, A., *Galaxy morphology in rich clusters: implications for the formation and evolution of galaxies.*, 1980, ApJ, 236, 351

Eke, V. R., et al., *Galaxy groups in the 2dFGRS: the group-finding algorithm and the 2PIGG catalogue*, 2004, MNRAS, 348, 866

Ferrami, G., & Wyithe, J. S. B., *A model for galaxy-galaxy strong lensing statistics in surveys*, 2024, MNRAS, 532, 1832

Fox, C., Mahler, G., Sharon, K., & Remolina González, J. D., *The Strongest Cluster Lenses: An Analysis of the Relation between Strong Gravitational Lensing Strength and the Physical Properties of Galaxy Clusters*, 2022, ApJ, 928, 87

Fujita, Y., *Pre-Processing of Galaxies before Entering a Cluster*, 2004, PASJ, 56, 29

Fukugita, M., Hogan, C. J., & Peebles, P. J. E., *The Cosmic Baryon Budget*, 1998, ApJ, 503, 518

Genzel, R., et al., *The Sins Survey of z ~2 Galaxy Kinematics: Properties of the Giant Star-forming Clumps*, 2011, ApJ, 733, 101

Gorenstein, M. V., Falco, E. E., & Shapiro, I. I., *Degeneracies in Parameter Estimates for Models of Gravitational Lens Systems*, 1988, ApJ, 327, 693

Graham, A. W., & Driver, S. P., *A Concise Reference to (Projected) Sérsic $R^{1/n}$ Quantities, Including Concentration, Profile Slopes, Petrosian Indices, and Kron Magnitudes*, 2005, PASA, 22, 118

Helsdon, S. F., & Ponman, T. J., *The intragroup medium in loose groups of galaxies*, 2000, MNRAS, 315, 356

Hernquist, L., *An Analytical Model for Spherical Galaxies and Bulges*, 1990, ApJ, 356, 359

Jullo, E., et al., *A Bayesian approach to strong lensing modelling of galaxy clusters*, 2007, NJPh, 9, 447

Koopmans, L. V. E., et al., *The Sloan Lens ACS Survey. III. The Structure and Formation of Early-Type Galaxies and Their Evolution since z ~1*, 2006, ApJ, 649, 599

Kormann, R., Schneider, P., & Bartelmann, M., *Isothermal elliptical gravitational lens models.*, 1994, A&A, 284, 285

Kormendy, J., & Ho, L. C., *Coevolution (Or Not) of Supermassive Black Holes and Host Galaxies*, 2013, ARA&A, 51, 511

Kravtsov, A. V., & Borgani, S., *Formation of Galaxy Clusters*, 2012, ARA&A, 50, 353

Leauthaud, A., et al., *A Weak Lensing Study of X-ray Groups in the Cosmos Survey: Form and Evolution of the Mass-Luminosity Relation*, 2010, ApJ, 709, 97

Limousin, M., Beauchesne, B., & Jullo, E., *Dark matter in galaxy clusters: Parametric strong-lensing approach*, 2022, A&A, 664, A90

Limousin, M., et al., *A new window of exploration in the mass spectrum: strong lensing by galaxy groups in the SL2S*, 2009, A&A, 502, 445

Lovisari, L., Ettori, S., Gaspari, M., & Giles, P. A., *Scaling Properties of Galaxy Groups*, 2021, Universe, 7, 139

Lovisari, L., Reiprich, T. H., & Schellenberger, G., *Scaling properties of a complete X-ray selected galaxy group sample*, 2015, A&A, 573, A118

LSST Science Collaboration, et al., *LSST Science Book, Version 2.0*, 2009, arXiv, arXiv:0912.0201

Massey, R., et al., *The behaviour of dark matter associated with four bright cluster galaxies in the 10 kpc core of Abell 3827*, 2015, MNRAS, 449, 3393

—, *Dark matter dynamics in Abell 3827: new data consistent with standard cold dark matter*, 2018, MNRAS, 477, 669

Meneghetti, M., et al., *The Frontier Fields lens modelling comparison project*, 2017, MNRAS, 472, 3177

Mihos, J. C., Harding, P., Feldmeier, J., & Morrison, H., *Diffuse Light in the Virgo Cluster*, 2005, ApJ, 631, L41

Mohammed, I., Liesenborgs, J., Saha, P., & Williams, L. L. R., *Mass-galaxy offsets in Abell 3827, 2218 and 1689: intrinsic properties or line-of-sight substructures?*, 2014, MNRAS, 439, 2651

Monna, A., et al., *CLASH: $z \sim 6$ young galaxy candidate quintuply lensed by the frontier field cluster RXC J2248.7-4431*, 2014, MNRAS, 438, 1417

Montes, M., *The faint light in groups and clusters of galaxies*, 2022, NatAs, 6, 308

Moore, B., et al., *Cold collapse and the core catastrophe*, 1999, MNRAS, 310, 1147

Navarro, J. F., Frenk, C. S., & White, S. D. M., *The Structure of Cold Dark Matter Halos*, 1996, ApJ, 462, 563

Newman, A. B., et al., *The Density Profiles of Massive, Relaxed Galaxy Clusters. I. The Total Density Over Three Decades in Radius*, 2013, ApJ, 765, 24

Oguri, M., *Fast Calculation of Gravitational Lensing Properties of Elliptical Navarro-Frenk-White and Hernquist Density Profiles*, 2021, PASP, 133, 074504

Overzier, R. A., *The realm of the galaxy protoclusters. A review*, 2016, A&A Rev., 24, 14

Peebles, P. J. E., *Large-scale background temperature and mass fluctuations due to scale-invariant primeval perturbations*, 1982, ApJ, 263, L1

Pillepich, A., Porciani, C., & Reiprich, T. H., *The X-ray cluster survey with eRosita: forecasts for cosmology, cluster physics and primordial non-Gaussianity*, 2012, MNRAS, 422, 44

Planck Collaboration, et al., *Planck 2018 results. VI. Cosmological parameters*, 2020, A&A, 641, A6

Pontzen, A., & Governato, F., *How supernova feedback turns dark matter cusps into cores*, 2012, MNRAS, 421, 3464

Pratt, G. W., et al., *The Galaxy Cluster Mass Scale and Its Impact on Cosmological Constraints from the Cluster Population*, 2019, Space Sci. Rev., 215, 25

Press, W. H., & Schechter, P., *Formation of Galaxies and Clusters of Galaxies by Self-Similar Gravitational Condensation*, 1974, ApJ, 187, 425

Rees, M. J., & Ostriker, J. P., *Cooling, dynamics and fragmentation of massive gas clouds: clues to the masses and radii of galaxies and clusters.*, 1977, MNRAS, 179, 541

Robotham, A. S. G., et al., *Galaxy and Mass Assembly (GAMA): the GAMA galaxy group catalogue (G^3Cv1)*, 2011, MNRAS, 416, 2640

Rubin, V. C., Ford, Jr., W. K., & Thonnard, N., *Rotational properties of 21 SC galaxies with a large range of luminosities and radii, from NGC 4605 (R=4kpc) to UGC 2885 (R=122kpc).*, 1980, ApJ, 238, 471

Saha, P., Sluse, D., Wagner, J., & Williams, L. L. R., *Essentials of Strong Gravitational Lensing*, 2024, Space Sci. Rev., 220, 12

Sérsic, J. L., *Influence of the atmospheric and instrumental dispersion on the brightness distribution in a galaxy*, 1963, Boletin de la Asociacion Argentina de Astronomia La Plata Argentina, 6, 41

Space Telescope Science Institute, *About Tiny Tim HST PSF Modeling*, 2004, About Tiny Tim HST PSF Modeling, `https://www.stsci.edu/hst/instrumentation/focus-and-pointing/focus/tiny-tim-hst-psf-modeling`

Springel, V., et al., *Simulations of the formation, evolution and clustering of galaxies and quasars*, 2005, Nature, 435, 629

Stark, D. P., et al., *The CASSOWARY spectroscopy survey: a new sample of gravitationally lensed galaxies in SDSS*, 2013, MNRAS, 436, 1040

Sun, M., et al., *Chandra Studies of the X-Ray Gas Properties of Galaxy Groups*, 2009, ApJ, 693, 1142

Swinbank, A. M., et al., *From star-forming spirals to passive spheroids: integral field spectroscopy of E+A galaxies*, 2012, MNRAS, 420, 672

Thanjavur, K., Crampton, D., & Willis, J., *Dark Matter Distribution in Galaxy Groups from Combined Strong Lensing and Dynamics Analysis*, 2010, ApJ, 714, 1355

Tinker, J., et al., *Toward a Halo Mass Function for Precision Cosmology: The Limits of Universality*, 2008, ApJ, 688, 709

White, S. D. M., & Frenk, C. S., *Galaxy Formation through Hierarchical Clustering*, 1991, ApJ, 379, 52

White, S. D. M., & Rees, M. J., *Core condensation in heavy halos: a two-stage theory for galaxy formation and clustering.*, 1978, MNRAS, 183, 341

Williams, L. L. R., & Saha, P., *Light/mass offsets in the lensing cluster Abell 3827: evidence for collisional dark matter?*, 2011, MNRAS, 415, 448

Wright, C. O., & Brainerd, T. G., *Gravitational Lensing by NFW Halos*, 2000, ApJ, 534, 34